UNIVERSIDAD DE CONCEPCIÓN
FACULTAD DE CIENCIAS FÍSICAS Y MATEMÁTICAS

The Main Sequence of Galaxy Evolution in the Local Universe

La Secuencia Principal de evolución de galaxias en el Universo Local

Por: Marcelo Andrés Figueroa Guerra.

Tesis presentada a la Facultad de Ciencias Físicas de Matemáticas de la Universidad de Concepción para optar al grado académico de Magíster en Ciencias con Mención en Física

Abril de 2021
Concepción, Chile

Profesor Guía: Neil Mark Nagar

© 2021, Marcelo Andrés Figueroa Guerra
Ninguna parte de esta tesis puede reproducirse o transmitirse bajo ninguna forma o por ningún medio o procedimiento, sin permiso por escrito del autor.

Se autoriza la reproducción total o parcial, con fines académicos, por cualquier medio o procedimiento, incluyendo la cita bibliográfica del documento

Dedicado a mi familia, amigos y a la comunidad Salesiana.

AGRADECIMIENTOS

Agradezco a mis compañeros de magister y administrativos, al comité evaluador, a los posdocs y profesores de la Universidad que contribuyeron a mi trabajo de tesis, en particular a mi profesor guía. Especiales agradecimientos a: imagine.gsfc.nasa.gov[1], Hubblesite.org[2] y NASA/IPAC Extragalactic Database (NED)[3] por proveer imágenes con valor científico que han sido útiles en la elaboración del presente informe de tesis. Gracias a Python.org[4] y Stackoverflow.com[5] por las herramientas de programación y soluciones facilitadas, las cuales hicieron posible este trabajo, y a Wikipedia[6] y StackExchange[7] por la difusión y soluciones sobre el lenguage LaTeX. Finalmente, agradezco a las bases de datos astronómicas que se han visto involucradas en este informe de tesis.

[1] https://imagine.gsfc.nasa.gov/science/objects/active_galaxies1.html
[2] https://hubblesite.org/contents/media/images/2008/16/2334-Image.html
[3] https://ned.ipac.caltech.edu/level5/March14/Conselice/Conselice1.html
[4] https://www.python.org
[5] https://stackoverflow.com
[6] https://es.wikipedia.org/wiki/Ayuda:Uso_de_LaTeX
[7] https://tex.stackexchange.com

Resumen

Contexto: Galaxias que forman estrellas en z ∼0-6 muestran una proporcionalidad entre su tasa de formación de estrellas (SFR) y masa estelar - la llamada Secuencia Principal (MS) de formación estelar. Esta puede ser descrita por una única ley de potencias que evoluciona con el corrimiento al rojo, con evidencia de una curvatura en masas estelares altas.

Metas: Aspiramos a caracterizar los parámetros de la MS de formacion estelar de bajo corrimiento al rojo (z≤0.03): pendiente, curvatura, dispersión y dependencia de otros parámetros.

Métodos: Usamos una muestra completa y bien definida de ∼40,500 galaxias de la muestra 2MRS, con fotometría de WISE de alta señal a ruido (S/N). Esta muestra está caracterizada extensivamente por morfología y la presencia de AGNs. La fotometría de WISE es usada para estimar masas estelares, SFRs, y morfología. Se usan ajustes Gaussianos en la MS observada para restringir la verdadera forma de la MS, su curvatura y dispersión. El contenido de AGNs y luminosidades bolométricas son usadas para desenmarañar los sesgos en la MS.

Resultados: Confirmamos que la fotometría de WISE estima de manera precisa masas estelares y SFRs, al compararle con otros métodos usados comúnmente. Nuestra MS resultante es mejor descrita por una ley de potencias quebrada: $\log \mathrm{SFR}_{\mathrm{low,MS}}/[\mathrm{M}_\odot/\mathrm{yr}] = 1.05 \log \mathrm{M}_\star/[\mathrm{M}_\odot] - 10.56$ at $\mathrm{M}_\star < 10.4\mathrm{M}_\odot$, and $\log \mathrm{SFR}_{\mathrm{high,MS}}/[\mathrm{M}_\odot/\mathrm{yr}] = 0.36 \log \mathrm{M}_\star/[\mathrm{M}_\odot] - 3.43$ at $\mathrm{M}_\star \geq 10.4\mathrm{M}_\odot$, con una dispersión intrínseca de 0.20-0.35 dex. Galaxias con AGN - especialmente AGNs de línea amplia - se encuentran preferencialmente en galaxias con altas SFRs específicas (SSFR); confirmamos que esto no es un sesgo introducido por la contaminación de AGN en las estimaciones de masas estelares y SFRs.

Conclusiones: Hemos mostrado que la fotometría de WISE caracteriza de forma precisa las masas estelares y SFRs en las galaxias locales, derivamos una caracterización precisa de la MS local y exploramos el rol de las AGNs en esta MS. Nuestros resultados son aprovechables únicamente en esta gran muestra que es estudiada intensivamente. Por lo tanto, ellos proveen no solamente una caracterización precisa de la MS local si no que también proporcionan una idea de los sesgos en otras muestras de alto corrimiento al rojo usadas para estudiar la

evolución de la MS.

Keywords – Secuencia Principal (MS), Formación Estelar (SF), Tasa de Formación Estelar (SFR), Evolución Secular, Núcleo Galáctico Activo (AGN).

Abstract

Context: Star-forming galaxies over z ∼0-6 show a proportionality between their star formation rate (SFR) and stellar mass - the so called Main Sequence (MS) of star formation. This can be described by a single power-law which evolves with redshift, with evidence for a turnover at high stellar masses.

Aims: We aim to precisely characterize the parameters of the low-redshift ($z \leq 0.03$) MS of star formation: slope, turnover, dispersion, and dependence on other parameters.

Methods: We use a well-defined and complete sample of ∼40,500 galaxies from the 2MRS sample, with high signal-to-noise (S/N) WISE photometry. This sample is extensively characterized by morphology and the presence of AGNs. WISE photometry is used to estimate stellar masses, SFRs, and morphology. Gaussian fits to the observed MS of this sample are used to constrain the true form of the MS, its turnover, and dispersion. AGN content and bolometric luminosities are used to disentangle biases in the MS.

Results: We confirm that WISE photometry accurately estimates stellar mass and SFRs, as compared to other commonly used methods. Our resulting MS is best described by a broken power-law: $\log \mathrm{SFR}_{\mathrm{low,MS}}/[\mathrm{M}_\odot/\mathrm{yr}] = 1.05 \log \mathrm{M}_\star/[\mathrm{M}_\odot] - 10.56$ at $\mathrm{M}_\star < 10.4\mathrm{M}_\odot$, and $\log \mathrm{SFR}_{\mathrm{high,MS}}/[\mathrm{M}_\odot/\mathrm{yr}] = 0.36 \log \mathrm{M}_\star/[\mathrm{M}_\odot] - 3.43$ at $\mathrm{M}_\star \geq 10.4\mathrm{M}_\odot$, with an intrinsic dispersion of 0.20-0.35 dex. Galaxies with AGNs - especially broad-line AGNs - are preferentially found in galaxies with higher specific SFRs (SSFRs); we confirm that this is not a bias introduced by AGN contamination on stellar masses and SFRs estimates.

Conclusions: We have shown that WISE photometry accurately characterizes stellar masses and SFRs in local galaxies, derived an accurate characterization of the local MS, and explored the role of AGNs in this MS. Our results are uniquely leverageable in this intensively studied large sample. They thus provide not only an accurate characterization of the local MS but also provide an idea of the biases in other higher redshift samples used to study the evolution of the MS.

Keywords – Main Sequence (MS), Star Formation (SF), Star Formation Rate (SFR), Secular Evolution, Active Galactic Nucleus (AGN).

Índice general

Índice de cuadros

Índice de figuras

Capítulo 1

Introduction

The parameter dependent Evolutionary Population Synthesis models (Charlot and Bruzual A, 1991; Bruzual A. and Charlot, 1993) concerning the time evolution based on *isochrone principle* allows one to compute the age-dependent distribution of stars in the Hertzsprung–Russell (HR) diagram. These models have become standard tools in the interpretation of galaxy colours and spectra. However, modern population synthesis models still shows large intrinsic uncertainties that arise from the poor understanding of some advanced phases of stellar evolution, such as the supergiant phase and the asymptotic giant-branch (AGB) phase (Charlot et al., 1996). On this phase stars are very bright and have a strong influence on integrated-light properties.

In the ultraviolet (UV) part of the electromagnetic spectrum, galaxy continuum show traces of stellar emission from young stars (type O, B), thus they represent a good measurement of star formation (SF) in galaxies (Kennicutt, 1988). The non-ionising UV continuum luminosity, where recently formed massive stars emit the bulk of their energy is often used as a direct star formation rate (SFR) indicator (Elbaz et al., 2007). Conversely, nebular emission luminosity from the Hα recombination line, which probes the hydrogen-ionising photons produced by the most massive and short-lived stars, is commonly used SFR indicator when spectroscopy is available (Kennicutt, 1988; Meurer et al., 1999; Kong et al., 2004; Buat et al., 2005; Wang et al., 2016; Kashino et al., 2019). More in the infrared (IR) wavelengths, aperture photometry from interstellar dust, e.g., Policyclic Aromatic Hidrocarbons (PAHs), is strongly related to SF and thus have been widely used

as SF tracer by current mid-infrared (MIR) surveys (Jarrett et al., 2013; Cluver et al., 2014, 2017), where fluxes from the diversity of PAHs species along the MIR wavelengths is accurately traced by the WISE bands. In this sense, SF in galaxies is traced by combining the observed UV continuum emission and the obscured SF traced by the IR emission from interstellar dust, by assuming energy conservation; such a principle argues that UV and optical starlight is absorbed by interstellar dust grains and then re-emitted in the IR and sub-millimeter wavelengths. However, not all the dust is remitted, giving place to dust attenuation effects. In nearby star-forming galaxies, the dust attenuation in the UV can vary from zero to several magnitudes. Thus, attenuation of the UV continuum by interstellar dust has motivated many works in literature, resulting in diverse extinction estimators, e.g., UV attenuation, IR/UV luminosity ratio or the power-law slope β ($f^{\alpha} \propto \lambda^{\beta}$) of the UV continuum (Meurer et al., 1999; Kong et al., 2004; Gil de Paz et al., 2007; Boquien et al., 2009; Kennicutt et al., 2009; Pannella et al., 2015; Salim et al., 2016; Wang et al., 2016; Salim et al., 2018).

A method widely used in literature to study SF is the SFR-$M_{\star}$ plane (Rodighiero et al., 2011), which relates the total stellar mass budget in a given galaxy to its SFR, being thus a measure of the evolution of the Universe through cosmic time. The most interesting feature of the SFR-$M_{\star}$ plane is the Main Sequence (MS) of galaxies (see for example, Fig. 1.0.1), which is evidence of SF activity driven by well known secular mechanisms like gas accretion, stellar outflows or interaction with the Interstellar Medium (ISM) material (e.g., Gehrz, 1989). The MS moves as a whole as SFRs increases with redshift (Tomczak et al., 2016; Thorne et al., 2020). On the other hand, merging mechanisms are believed to cause more violent SF and gas depletion episodes (Toomre and Toomre, 1972; Calderón-Castillo et al., 2019; Ogle et al., 2019), where galaxies which interact with the each other through tidal forces (see Fig. 1.0.2), enhancing SF in MS galaxies (normal star-forming) and turning them into starburst (SB), with up to 100 times the normal levels of SFR (Rodighiero et al., 2011). These SB episodes could be a result of merger activity, as it has been evidenced by the MS of Fig. 1.0.3. Further, at earlier cosmic times (z>1), it is thought that SB galaxies in merging processes are more frequent (Noeske et al., 2007), leading to the peak of larger mergers at redshifts 1 to 2 (Wright et al., 2010). Out to redshift ∼2.5, SBs are known to represent only the 2 % of the total galaxy population and about 20 % of all SF (Brinchmann

et al., 2004; Rodighiero et al., 2011; Orellana et al., 2017).

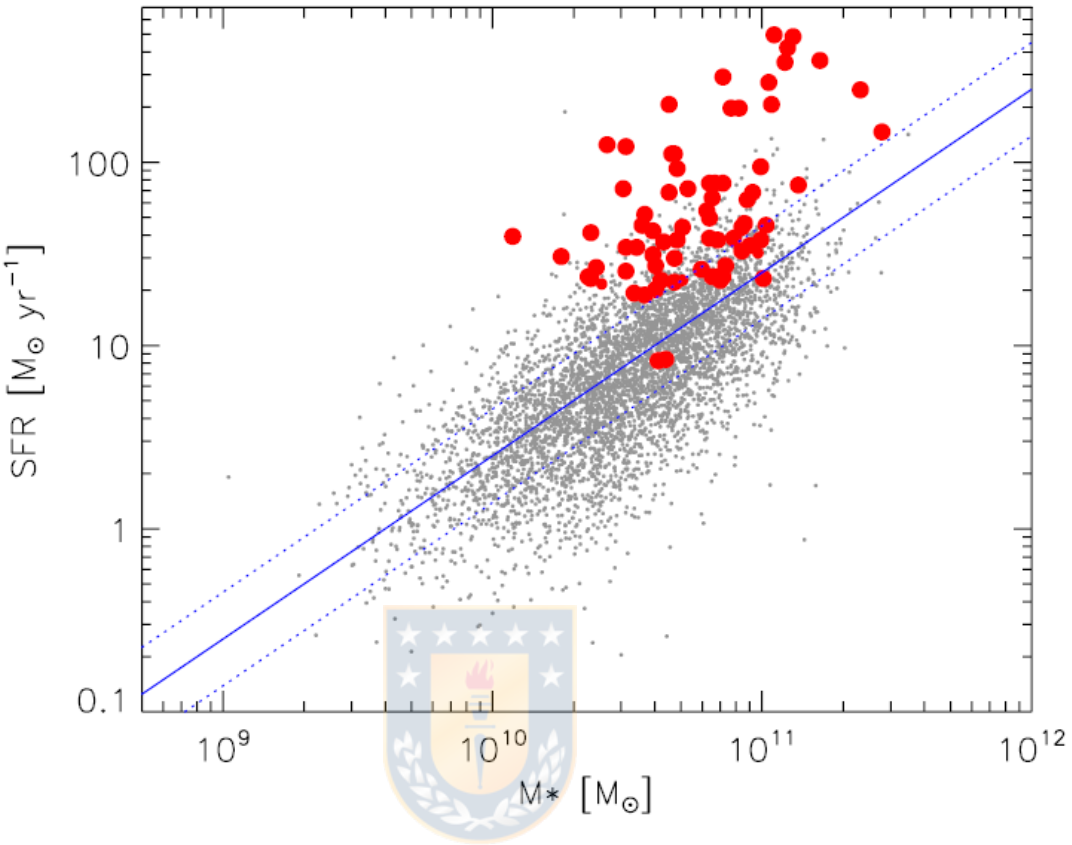

Figura 1.0.1: The SFR-M$_\star$ plane and Main Sequence (MS) of Elbaz et al. (2011) for AKARI galaxies at z$\sim$0. The best fit to this relation is a one-to-one correlation. Galaxies classified as compact are marked with red filled dots. The solid line corresponds to the MS: SFR $\propto$ M$_\star/[4 \times 10^9 M_\odot]$. Dotted lines: distribution around the sliding median (0.26 dex).

Main Sequence has been investigated from redshift $\sim$0 up to $\sim$9, e.g., Brinchmann et al. (2004); Elbaz et al. (2007); Santini et al. (2009); Noeske et al. (2007); Genzel et al. (2010); Rodighiero et al. (2010); Peng et al. (2010); Karim et al. (2011); Popesso et al. (2011); Wuyts et al. (2011); Rodighiero et al. (2011); Elbaz et al. (2011); Whitaker et al. (2012); Guo et al. (2013); Speagle et al. (2014); Santini et al. (2014); Rodighiero et al. (2014); Whitaker et al. (2014); Whitaker et al. (2014); Steinhardt et al. (2014); Vogelsberger et al. (2014); Genel et al. (2014); Mancini et al. (2015); Tacchella et al. (2015); Gavazzi et al. (2015); da Cunha et al. (2015); Henriques et al. (2015); Chang et al. (2015); Whitaker et al. (2015); Pannella et al. (2015); Renzini and Peng (2015); Schreiber et al. (2015); Lee

[1]https://hubblesite.org/contents/media/images/2008/16/2334-Image.html

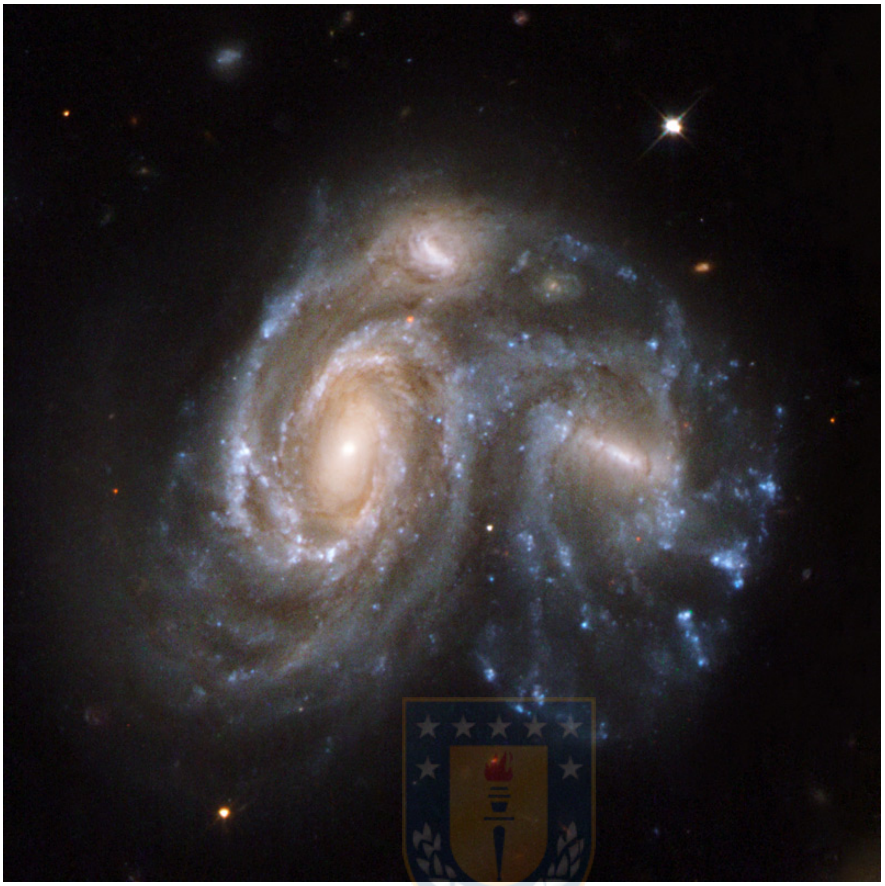

Figura 1.0.2: The merging system NGC 6050/IC 1179 (Arp 272)[1]arises from the collision between two spiral galaxies, NGC 6050 and IC 1179, which is part of the Hercules Galaxy Cluster, located in the constellation of Hercules. The two spiral galaxies are linked by their arms. This image is part of a large collection of 59 images of merging galaxies taken by the Hubble Space Telescope.

et al. (2015); Kurczynski et al. (2016); Davies et al. (2016); Tomczak et al. (2016); Jarrett et al. (2017); Orellana et al. (2017); Cluver et al. (2017); Whitaker et al. (2017); Pearson et al. (2018); Davies et al. (2019); Calderón-Castillo et al. (2019); Popesso et al. (2019a); Popesso et al. (2019b); Ogle et al. (2019); Kashino et al. (2019); Puglisi et al. (2019); Thorne et al. (2020).

Main Sequence depends on a set of parameters that describe its most important features, usually these evolve with stellar mass or cosmic time, i.e., intrinsic scatter, turnover mass/characteristic mass, slope and normalization. Intrinsic scatter of the MS is the statistical deviation of either SFRs or specific SFRs (SSFR); the latter case has been studied by Rodighiero et al. (2011), who performed gaussian fits to a sample of star-forming galaxies to rule out biases on these, i.e., SB populations (see Fig. 1.0.5). At z=0, some works find constant intrinsic scatter ∼0.17-0.3 dex

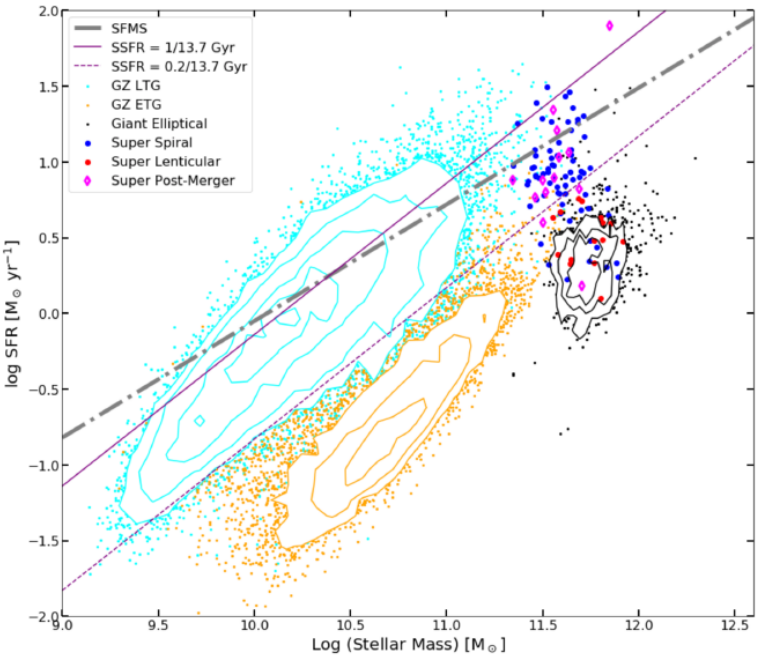

Figura 1.0.3: The SFR-$M_\star$ plane and MS of Ogle et al. (2019), whose WISE-based SFRs and masses in stars of super disks, post-mergers, and giant ellipticals (OGC galaxies) are compared to Galaxy Zoo late-type and early-type galaxies (Alatalo et al., 2014; Schawinski et al., 2014, GZ LTGs and ETGs), with these morphologies corresponding to the most massive versions of the commonly known galaxy types. The thick dot-dashed line indicates the star-forming MS at z∼0 (Elbaz et al., 2007), which has been shifted downward by 0.22 dex to match the WISE-based SFR estimates of Chang et al. (2015). The dashed and purple solid lines indicate SFRs in a range where active star-forming galaxies would double their masses in stars in 1-5 times the current age of the Universe. There is no sharp dividing line between super spirals and super lenticulars. Because super spirals are so massive, not even the ones with the highest SFRs and IR luminosities are global SBs. Most of the super post-mergers have SFRs that formally put them on the star-forming MS.

(Whitaker et al., 2012; Schreiber et al., 2015), while other authors assess a roughly monotonic increase of scatter with redshift and stellar mass from 0.3-0.45 dex (Popesso et al., 2019a). Conversely, normalization of the MS is found to vary between ∼-12.97 and -2.97 (Whitaker et al., 2012; Santini et al., 2014; Renzini and Peng, 2015; Popesso et al., 2019a). While slope of the MS varies widely in the literature and depends on the best-fit method used, spanning from 0.6-1.45 (Brinchmann et al., 2004; Peng et al., 2010; Elbaz et al., 2011; Wuyts et al., 2011; Whitaker et al., 2012; Santini et al., 2014; Renzini and Peng, 2015) for a single power-law. Other authors have determined a bending in the MS at high masses,

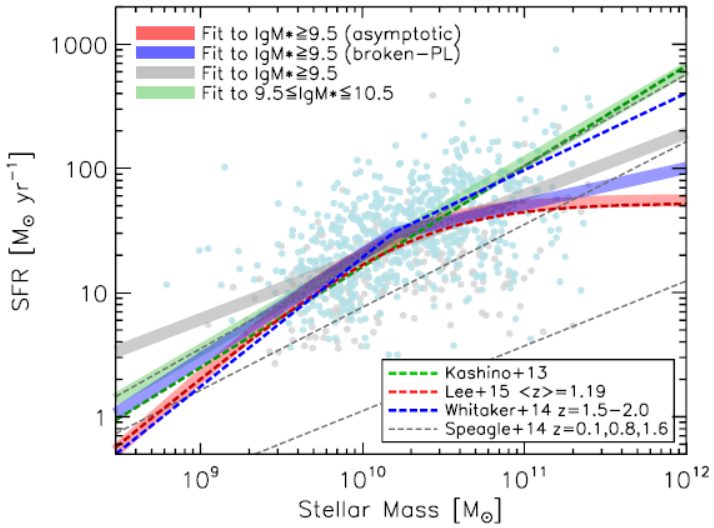

Figura 1.0.4: SFR-$M_\star$ plane and MS of of Kashino et al. (2019) for FMOS objects, in comparison to literature measurements. Pale-colored circles indicate FMOS objects. The thick solid curves indicate the best-fit relations to the FMOS data: power-law fits (gray), asymptotic function fit (red), and broken power-law fit (blue). Colored dashed-lines indicate literature measurements: a fit to a subset of the FMOS sample by Kashino et al. (2013, green), broken power-law fit at 1.5≤z≤2.0 by Whitaker et al. (2014, blue), and asymptotic function fit at median <z>=1.19 by Lee et al. (2015, red). Three gray dashed-lines indicate empirically parameterized relations at z=0.1, 0.8, and 1.6 (top to bottom) derived by Speagle et al. (2014). The power-law fit from Kashino et al. (2019) is fully consistent with previous results from Kashino et al. (2013) and redshift compilations derived by Speagle et al. (2014). On the other hand, a fit to the entire mass range ($\log M_\star/\mathrm{M}_\odot \geq 9.5$) yields a shallower slope. In addition, the broken power-law fit to the FMOS data yields a shallower high mass slope ($a_{\mathrm{high}} = 0.29$) than the result from Whitaker et al. (2014), but that is rather similar to the power-law slope 0.27 found by Lee et al. (2015). In contrast, the best-fit with an asymptotic function is in good agreement with results from Lee et al. (2015).

which is better described by a broken power-law (Popesso et al., 2019a) or a non-linear best-fit method (Gavazzi et al., 2015; Schreiber et al., 2015; Thorne et al., 2020) with low mass slopes spanning from 0.76-1 and high mass slopes from 0.2-0.41. These methods usually define a turnover mass to separate the MS into a low and high mass ends (Gavazzi et al., 2015; Schreiber et al., 2015; Popesso et al., 2019a; Thorne et al., 2020), spanning from $10^{9.45} - 10^{10.5}\mathrm{M}_\odot$. Fig. 1.0.4 summarize the different features of the MS mentioned here, as the different methods available in literature that has been used to derive a MS so far.

At high redshift, some works find a constant intrinsic scatter, e.g., spanning from

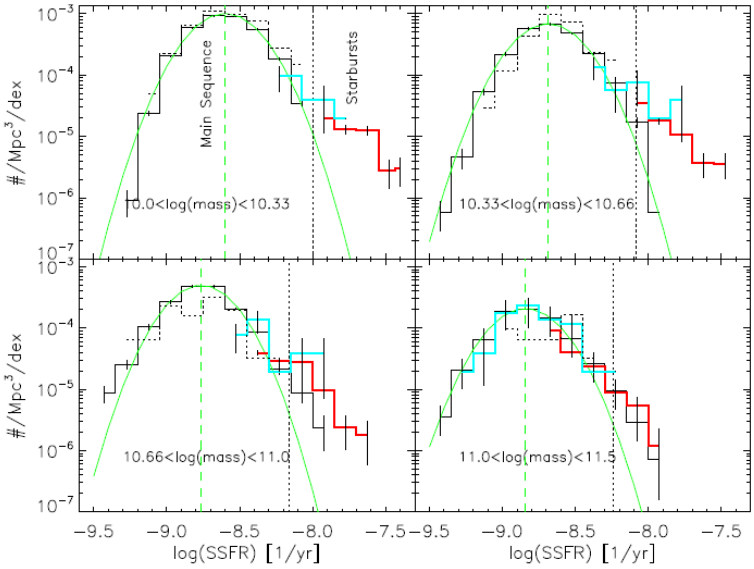

Figura 1.0.5: Distribution of the specific Star Formation Rates (SSFRs) for the four SF galaxy samples from Rodighiero et al. (2011) in four mass bins, corrected by the corresponding co-moving volumes and after accounting for volume and selection incompleteness. The black-dotted, black solid, cyan and red histograms correspond to the BzK samples defined by Daddi et al. (2007). The error bars are Poissonian, resulting in a nearly constant $\sigma = 0.24$ dex, whilst the green curves show the Gaussian fits to the black solid histograms. Green-dashed vertical lines represent a 0.6 dex dispersion. The SSFR distributions from the four samples agree within the errors (Poisson) in the regions of overlap. Deviations from the Gaussian distributions start to be clearly detected at SSFRs 0.6 dex above the average, which is the adopted threshold to define on-main sequence and off-main sequence galaxies. Such deviations are less obvious in the highest mass bin. The distribution functions in this Figure allow us to define MS outliers, i.e., SB galaxies.

∼0.25-0.39 dex (Rodighiero et al., 2011; Whitaker et al., 2012; Steinhardt et al., 2014; Schreiber et al., 2015; Chang et al., 2015), while other authors assess a scatter evolving with redshift between ∼0.08-0.39 dex (Whitaker et al., 2015; Kurczynski et al., 2016; Pearson et al., 2018; Popesso et al., 2019b) and stellar mass from 0.17-0.39 dex (Guo et al., 2013; Popesso et al., 2019b; Kashino et al., 2019). An example of this evolution is shown in Fig. 1.0.6, where we see the variety of scatters up to redshift ∼2.5, found by Popesso et al. (2019b). Conversely, normalization of the MS vary between ∼-12.97 and -5.5 mostly increasing (Genzel et al., 2010; Elbaz et al., 2007; Santini et al., 2009; Rodighiero et al., 2011; Guo et al., 2013; Mancini et al., 2015; Chang et al., 2015; Kurczynski et al., 2016) or decreasing with redshift (Santini et al., 2014), depending on the best-fit method used (although there is some discrepancy among authors). SF increases with

redshift as $\propto (1+z)^{\gamma}$, with γ spanning from $\sim$1.8-4.12 (Pannella et al., 2015; Rodighiero et al., 2010; Karim et al., 2011; Whitaker et al., 2014; Lee et al., 2015; Popesso et al., 2019b). While slope of the MS varies widely in the literature and depends on the best-fit method used, determining a mostly increasing slope with redshift (although differing among authors) and spanning from 0.43-1.92 (Elbaz et al., 2007; Santini et al., 2009; Genzel et al., 2010; Karim et al., 2011; Rodighiero et al., 2011; Wuyts et al., 2011; Guo et al., 2013; Santini et al., 2014; Steinhardt et al., 2014; Pannella et al., 2015; Whitaker et al., 2015; Chang et al., 2015; Mancini et al., 2015; Kurczynski et al., 2016; Pearson et al., 2018; Kashino et al., 2019) if a single power-law is used. Other authors determined a bending MS at high masses, which is better described by a broken power-law (Whitaker et al., 2014; Lee et al., 2015; Popesso et al., 2019a; Kashino et al., 2019) or well, a non-linear best-fit (Whitaker et al., 2014; Lee et al., 2015; Gavazzi et al., 2015; Tomczak et al., 2016; Schreiber et al., 2015; Kashino et al., 2019; Thorne et al., 2020) with low mass slopes spanning from 0.76-1.3 and high mass slopes from 0.14-0.8. They also determined a turnover mass of the bending MS, being roughly constant and spans between 10^{10}-$10^{10.5}$M$_{\odot}$ (Lee et al., 2015; Whitaker et al., 2015; Schreiber et al., 2015; Kashino et al., 2019; Popesso et al., 2019b), while other findings assess a mostly increasing turnover with increasing redshift (Whitaker et al., 2014; Gavazzi et al., 2015; Tomczak et al., 2016; Lee et al., 2015; Thorne et al., 2020), spanning from $10^{9.45}$-$10^{10.11}$M$_{\odot}$. Some authors find an indistinguishable turnover mass at high redshift (Whitaker et al., 2015; Schreiber et al., 2015), in particular, Gavazzi et al. (2015) have determined that such a turnover evolves with redshift as $\propto (1+z)^2$.

The Active Galactic Nucleii (AGN, Fig. 1.0.7) outflow mechanisms related to their total radiative output and kinetic power has been widely studied in literature (Antonucci, 1993; Dumas et al., 2007; Punsly and Zhang, 2011; Scott and Stewart, 2014; Oh et al., 2015; Ezhikode et al., 2017; Brightman et al., 2017; Audibert et al., 2017), however, how AGN power can bias SF luminosity in galaxies (Elbaz et al., 2011; Mingo et al., 2016) is still not fully understood. Indeed, AGN outflows may dominate the radiative spectrum of the galactic nucleus beyond 20μm, i.e., this contribution becomes important when reaching 22-24μm MIR bands (Netzer et al., 2007; Elbaz et al., 2011; Jarrett et al., 2013; Schreiber et al., 2015; Popesso et al., 2019b), reaching up to 75 % of the UV-to-IR emission, as shown by Hayward

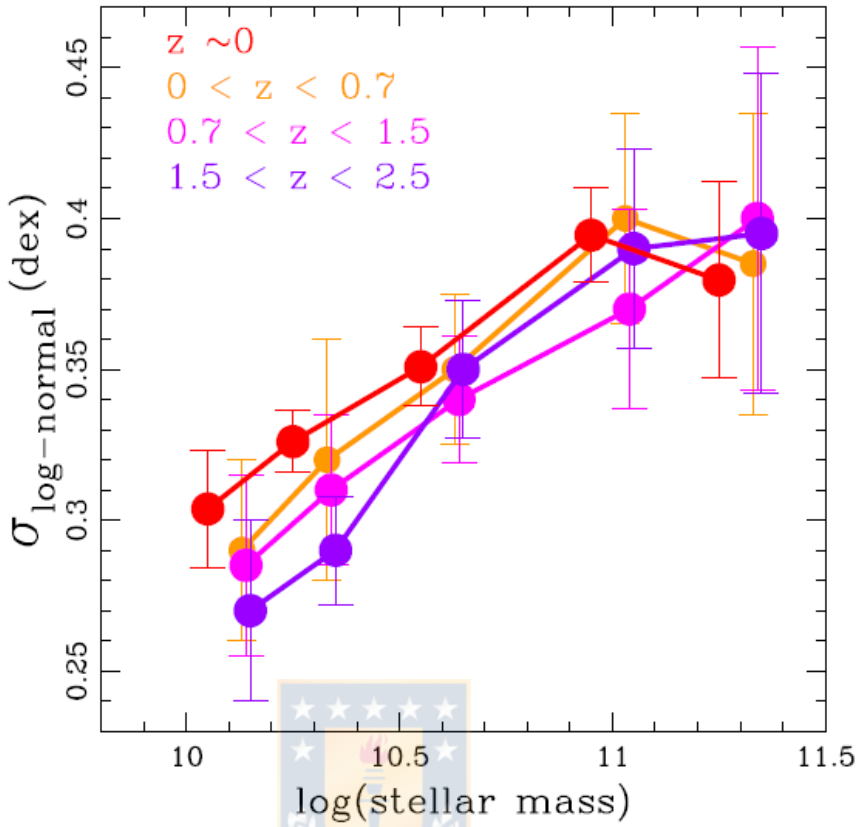

Figura 1.0.6: Evolution of the Main Sequence scatter at different redshifts spanning from z ∼0 to z∼2.5, determined by Popesso et al. (2019b). This scatter is measured as the dispersion of the log-normal component, which is increasing as a function of stellar mass from ∼0.28±0.03 dex at $10^{10}M_{\odot}$ to ∼ 0.39±0.03 at $10^{11}M_{\odot}$. Due to the lower statistics of the high redshift distributions with respect to the local one, the error bars are larger and the trend is significant only at the 2σ level.

and Smith (2015), with 12μm flux being much less affected by AGN-heated hot dust than the 22μm (Salim et al., 2016).

Several colour cutoffs have been proposed to identify galaxies by their morphology or AGN content (e.g., Lake et al., 2012; Mateos et al., 2012; Stern et al., 2012; Assef et al., 2013; Mingo et al., 2016; Marleau et al., 2017). In this work we use the classification by WISE colors from Jarrett et al. (2011); Cluver et al. (2014), that allow us to derive a new morphology of the 2MRS galaxies, relative to their positions in the WISE color-color diagram (see Fig. 1.0.9). This classification is dependent on the morphology derived by Huchra et al. (2012), which is based on

[2]https://imagine.gsfc.nasa.gov/science/objects/active_galaxies1.html

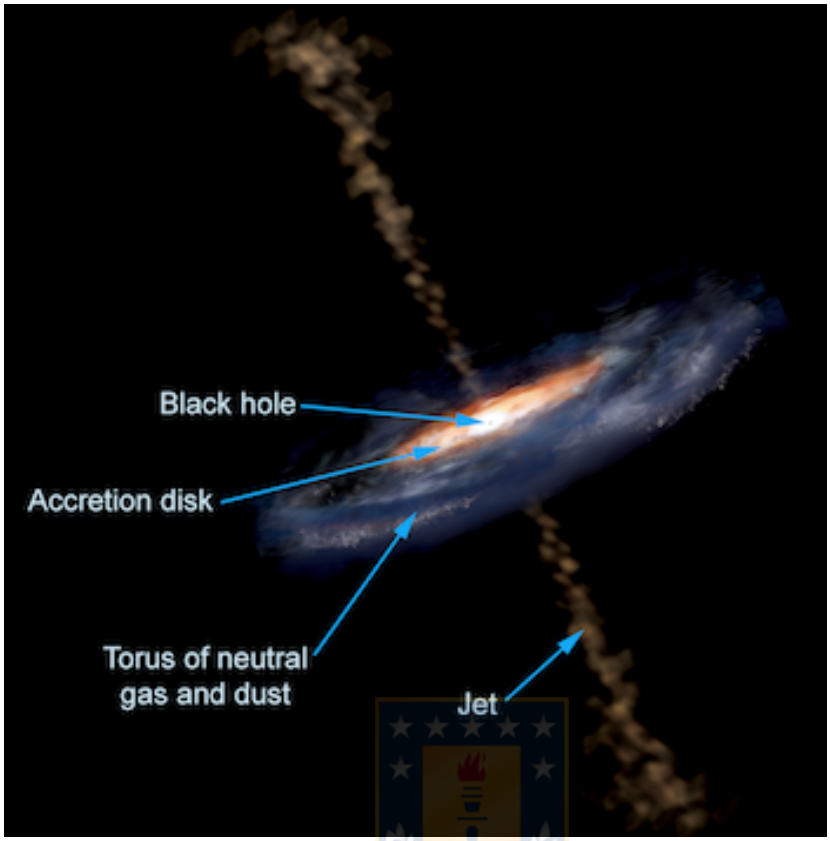

Figura 1.0.7: This illustration shows the different features of an Active Galactic Nucleus (AGN)[2], at very short distances from the central nucleus. These active galaxies have a small core of emission embedded by the AGN torus, at the center of an otherwise typical galaxy. In an AGN, the extreme luminosity emitted is powered by accretion onto a supermassive black hole, and as the material falls on it. In about one out of ten AGN, the black hole and accretion disk produce narrow beams of energetic particles and ejects them outward in opposite directions away from the disk. Credit: Aurore Simonnet, Sonoma State University.

a modified Hubble Sequence (shown in Fig. 1.0.8) from de Vaucouleurs (1963).

Since previous decades and more intensively in the last years, SF in galaxies has been studied by several astronomical surveys at different regions of the electromagnetic spectrum, covering the entire observable sky and improving the resolution of their predecessors. In the IR wavelengths, early observations of the cosmic cirrus were performed by The Infrared Astronomical Satellite (IRAS, Neugebauer et al., 1984; Bei, 1988), which was launched in January of 1983. IRAS is a deep field all-sky survey whose objective was to search for astrophysical objects with angular extents less than 0⁄5 0⁄5, 0⁄5, 1.0′, and 2.0′ in the scan direction at

[3]https://ned.ipac.caltech.edu/level5/March14/Conselice/Conselice1.html

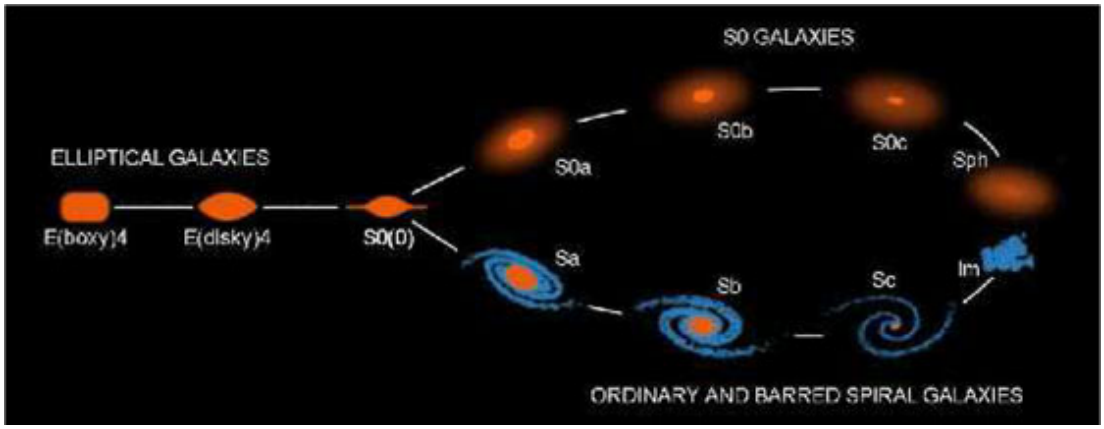

Figura 1.0.8: A modern form of the Hubble Sequence[3]showing the sequence of ellipticals and SOs, and the Hubble "tuning fork" in spirals, which corresponds to the differential between spirals with and without bars. The elliptical sequence is determined by the overall shape of the galaxy, while spiral classifications are divided into different types (a-c) depending upon how wound-up spiral arms are, how large the bulge relative to the disk is, and how smooth the spiral arms in the spirals arm. Also shown is the extension of this sequence to dwarf spheroidal galaxies and irregular galaxies, both of which are lower mass systems (Kormendy and Bender, 2012).

12μm, 25μm, 60μm, and 100μm bands of the IR spectrum, using a resolution of 8 arc-minutes and typical position uncertainties around 2″ to 6″ in-scan. The data from observations was released in a unique catalog called IRAS Catalog of Point Sources (PSC, Bei, 1988), for a total of 245,889 sources in its version 2.0, with specific versions through the time, e.g, the IRAS Catalog of Galaxies and Quasars, having a total of 11,444 entries. The reliability of IRAS (>99.8 %) make it a nice complement to other catalogs in the IR bands, also because it covers the 98 % of the unconfused regions of the sky. Therefore, IRAS is useful for observations of SF activity when in combination with WISE MIR bands.

The Two Micron All-Sky Survey (2MASS, Skrutskie et al., 2006) mapped the entire sky in the bands H, J and K_s (see Fig. 1.0.10), avoiding biases in optical and IR affecting all-sky surveys before 2MASS and reducing extinction effects by about a $\times 10$ factor. The 2MASS photometric pipeline produced an Extended-Source Catalog (XSC, Jarrett et al., 2000; Jarrett, 2004) has $\sim 10^6$ objects with $K_s \leq 13.5$ mag. This allow us to construct a uniform, all-sky three-dimensional map of galaxies of the Local Universe. 2MASS shows a good example of the zone-of-avoidance, since its XSC version is only limited by stellar confusion near the galactic center (Huchra et al., 2005). In this work, we mainly base our study

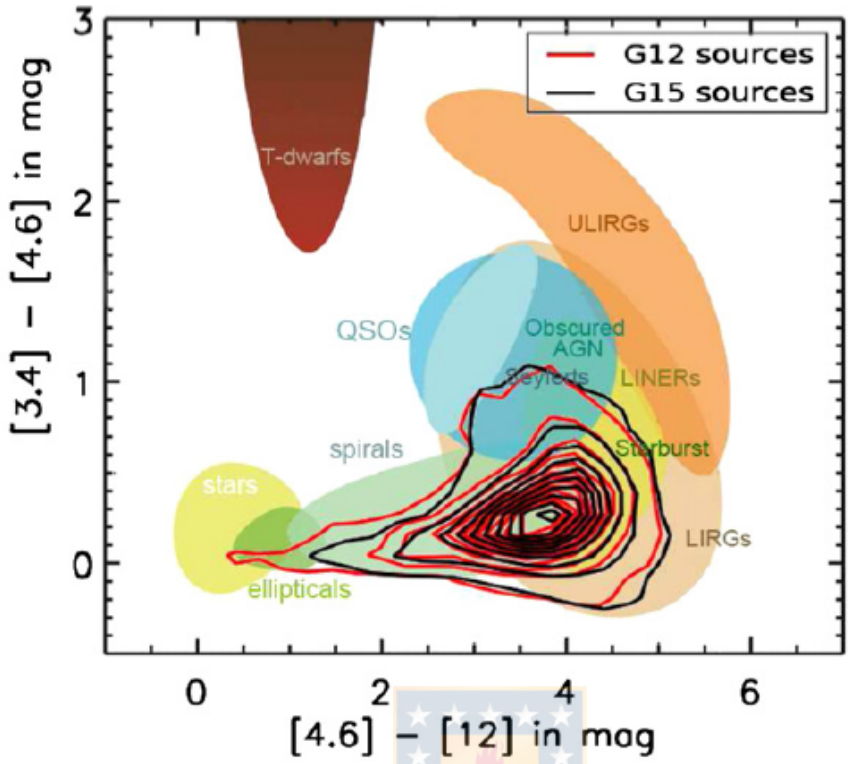

Figura 1.0.9: The WISE color-color diagram of Cluver et al. (2014), with "k-corrected" WISE colors from sources in the GAMA fields G12 and G15 (black and red contours). The background illustrates the locations of interesting classes of objects at different redshifts; stars and early-type galaxies (ETGs) have colors near to zero, QSOs have relatively blue colors in the shorter bands, whilst ultra-luminous infrared galaxies (ULIRGs) have the reddest overall colors. The shortest bands are sensitive to the evolved stellar population and hot dust, the latter indicative of AGN or SB activity. Conversely, 12μm band is dominated by the 11.3μm PAH, as well as the dust continuum, sensitive to star formation. Heavily obscured galaxies like ULIRGs are absent in this diagram due to the insensitivity (selective extinction) of SDSS and GAMA optical catalogs.

of local SF in the 2MRS-XSC release.

The successor of IRAS and the Cosmic Background Explorer (COBE), the Wide-field Infrared Survey Explorer (WISE, Wright et al., 2010) was launched in December of 2009, and whose main task was to perform observations of the entire sky at its four MIR bands: 3.4μm, 4.6μm, 12μm, and 22μm with angular resolutions are 6.″1, 6.″4, 6.″5, and 12.″0, respectively. This 40 cm telescope has a significantly higher sensitivity than IRAS in the MIR range, where saturation starts to appear when sources are brighter than approximately 8.1, 6.7, 3.8, and −0.4 mag at 3.4μm, 4.6μm, 12μm, and 22μm, respectively. WISE catalogs are

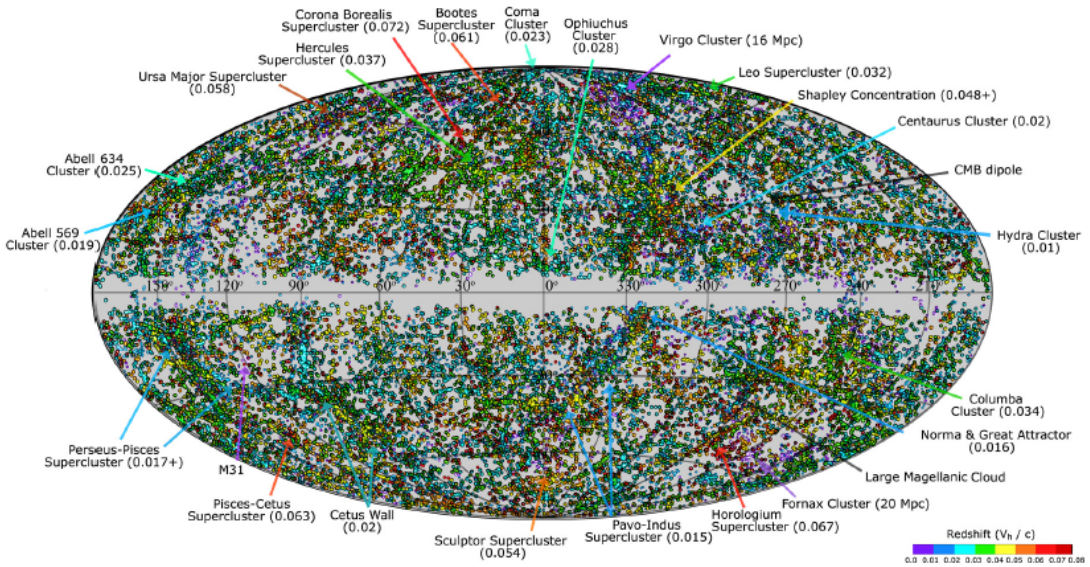

Figura 1.0.10: Distribution on the sky of galaxies in the 2MRS catalog (Huchra et al., 2012), spanning the entire redshift range covered by the survey, with the major structures of the Local Universe labeled. This map uses Galactic coordinate projections.

published by the NASA/IPAC Infrared Science Archive (IRSA), they had their first release in April of 2011 (Preliminary Data release) and their last released were in March of 2012 (All-Sky Data release), with different sky sizes covered at different epochs. Mainly, these results extend the 2MASS survey into the thermal IR. WISE has many catalogs published by IRSA but our paper is based only in the results of the ALLWISE DATA release, which was published in November of 2013, so posterior data through the called "near-Earth object" + WISE released data (NEOWISE, 2018) have an improved coverage of the sky and improved calibrations procedures applied to the previous data, although mainly focused on small objects of our solar system.

The Sloan Digital Sky Survey (SDSS, York et al., 2000), has a 2.5 meter telescope at Apache Point Observatory, New Mexico, destined to map the sky at the optical (u, g, r, i, z bands). It started operations in May of 2000, with its first data release DR1, through SDSS-I (2000-2005) project and ending up with DR7 through the SDSS-II (2005-2008) project, which includes DR8 to DR10 data releases. SDSS-III (2008-2014) and the current SDSS-IV (2014-2020), which involves other three surveys each one covering different spectra (eBOSS, APOGEE-2 and MaNGA) and the SDSS-V (2020). Every project has involved "Prior Surveys" that allowed

to map sky for diverse purposes, like SDSS Data Release 16 (DR16[4]), through August of 2018, which is made of cumulative data releases: DR12, DR13, DR14 and DR15.

The Galaxy Evolution Explorer (GALEX, Bianchi et al., 2003; Gil de Paz et al., 2004) satellite, launched in Abril of 2003, observes the Local Universe in near-ultraviolet (NUV) and far-ultraviolet (FUV) wavelengths with an angular resolution of 4.″3 and 5.″3 respectively. The Nearby Galaxy Survey (NGS, Gil de Paz et al., 2007), is a compendium of 1,034 nearby galaxies with angular diameters larger than 1′, observed by GALEX in FUV (1,350-1,780 Å) and NUV (1,770-2,730Å) bands. In this work we use the GALEX data sets available in literature, these correspond to late General Releases 6 and 7 (GR6/GR7) from the public Multi-Mission archive at the Space Telescope Science Institute (MAST), which is the major GALEX data release (2010).

The NASA-Sloan Atlas (NSA) is a catalog of 640,000 galaxies local galaxies at redshift $z < 0.05$ from the DR8 release data (SDSS, Blanton et al., 2011), and GALEX GR6 photometric data, so its coverage includes u, g, r, i, z optical bands and NUV and FUV bands. The NSA includes additional data from the following catalogs: NASA Extragalactic Database (NED), Six-degree Field Galaxy Redshift Survey (6dFGS), Two-degree Field Galaxy Redshift Survey (2dFGS), ZCAT and ALFALFA.

The GALEX-SDSS-WISE Legacy Catalog (GSWLC, Salim et al., 2016) is a catalog of ∼700,000 galaxies with physical properties like SFRs based on MIR measurements of WISE-4 (W4) band, UV/optical Spectral Energy Distribution (SED) fitting and stellar masses, with SDSS redshifts below 0.3 and magnitudes < 18. It also includes galaxies with GALEX footprints, regardless of a UV detection, that at the same time covers the 90 % of the 1.″3 resolution of the SDSS. These catalogs have 3 variants depending on the deep of the sample, with GSWLC-1 described by Salim et al. (2016) and a second version which is explained by Salim et al. (2018), which has improved dust attenuation curves and more accurate SFRs. GSWLC was built using data from SDSS Main Galaxy Sample (MGS, Strauss et al., 2002) which is an spectroscopic survey of the Local Universe.

In this thesis report we use complementary data sets and catalogs, which we

[4]https://www.sdss.org/dr16/

compare to our WISE-derived stellar masses and SFRs for consistency, thus, this help us to identify parameters that could bias our data sets. Most of estimations on galaxy stellar mass derived in past literature by da Cunha et al. (2015) have been based on accurate predictions of the galaxy SED (see Fig. 1.0.11). In our work we calculate stellar masses from current available calibrations of the mass-to-light ratio based on WISE photometric bands (Cluver et al., 2014), then we compare them to those data sets from Chang et al. (2015) and Salim et al. (2016). Conversely, we obtain our main set of SFRs based on WISE photometry, by using a set of equations described by Cluver et al. (2017). Independently, SFRs based on IRAS FIR bands are calculated using the total IR calibrations from Kennicutt (1998) and Orellana et al. (2017), whilst GALEX deep UV observations provided by the NSA catalog allow us to calculate IR-corrected SFRs in both NUV and FUV bands, which is achieved by calibrations presented by Wang et al. (2016).

Local MS (z$\sim$0) has been studied in previous works with a diversity of large and complete data sets, such as those based on SDSS photometry, e.g., Brinchmann et al. (2004); Renzini and Peng (2015); optical+21cm emission line, e.g, Gavazzi et al. (2015); multi-wavelength analyses, e.g., Elbaz et al. (2011); Wuyts et al. (2011); Whitaker et al. (2012); Schreiber et al. (2015); Thorne et al. (2020). Most of past works on the Local Universe have determined that the MS is better represented by a power-law function (in logarithmic scales), with some having found a bending at the high mass end, which is instead better described by a broken power-law or similarly, a non-linear function. In particular, Popesso et al. (2019a) combine SDSS Hα spectroscopy with WISE MIR photometry, to determine that local MS can be represented as a broken power-law function. Here we show that bending of the z$\sim$0 MS can be reproduced purely by MIR photometry from WISE bands, thus reproducing previous results like the one of Popesso et al. (2019a), and adding better concordance to their low mass MS with current high-redshift studies.

In this work we study SF of isolated galaxies in the MS of galaxies up to redshift $<z>\sim$ 0.03. For this purpose, we create a parent sample based on 2MRS galaxies, in combination with the WISE MIR photometry, thus providing us a large sample of galaxies with a high completeness in both, stellar masses and SFRs that is independent of previous researches on MS in the Local Universe, in particular for low mass galaxies. By using a similar methodology to the ones proposed by e.g.,

Lee et al. (2015); Whitaker et al. (2015); Popesso et al. (2019a), we determine that our MS is best described by a broken power-law with a bending at high stellar masses and this is purely assessed by monochromatic observations from the WISE bands.

This thesis report has been divided into four chapters; at the same time, these have been divided into sections, whose order is the following: chapter 2, where we present our 2MRS parent galaxy sample and other complementary galaxy samples as the different signal-to-noise cuts performed to our data samples; and chapter 3, where we show the different methods used in this thesis work related to the SFP and the MS, as their respective results. In section 3.1 we explain our method to classify the 2MRS sample by WISE colors, for this we explore the WISE color-color parameter space, thus we introduce our normal star-forming sample of galaxies. In section 3.2 we carry out stellar mass calculations based on WISE-1 band calibrations derived by Cluver et al. (2014), then we compare them with stellar mass estimations in literature; in section 3.3 we motivate the use of WISE-3 and WISE-4 in-band photometry as our main tracers of SF by using calibrations performed by Cluver et al. (2017), plus other UV and IR SF tracers, namely, we use total IR calibrations for UV SFRs presented in Wang et al. (2016). In section 3.4 we show our results on the SFP based on the SF tracers and stellar masses from section 3.2 and 3.3, respectively. Then, we describe our results on the MS of star-forming galaxies and our procedure to derive its intrinsic scatter. Section 3.5 show the evolution of SSFR with redshift in our MS galaxies and in section 3.6 we perform a classification of the same sample by AGN content, then we investigate the possible links between AGN total radiative output and their bias introduced to the SF in our sample of galaxies. After this, in sections 3.7 and 3.8 we briefly discuss how the presence of SB galaxies can bias our MS. Lastly, we carry out comparisons between our MS results and the different MS available in literature, in both, local and high redshift (chapter 4). Appendix A is complementary to section 3.3 and show comparative diagrams between our W3-based SFRs and our set of multi-band SF tracers; in appendix B we show a SFP based on the W4 band, relative to our results of 3.4, whilst appendix C complements the arguments introduced in section 3.1 related to our morphology classification based on WISE colors.

In this work we adopt a ΛCDM cosmology with Hubble constant H_0 =

72 km/s/Mpc and parameters $\Omega_{\mathrm{M}} = 0.3$ and $\Omega_{\Lambda} = 0.7$. SFRs are based on a Kroupa's Initial Mass Function (Kroupa, 2001, IMF).

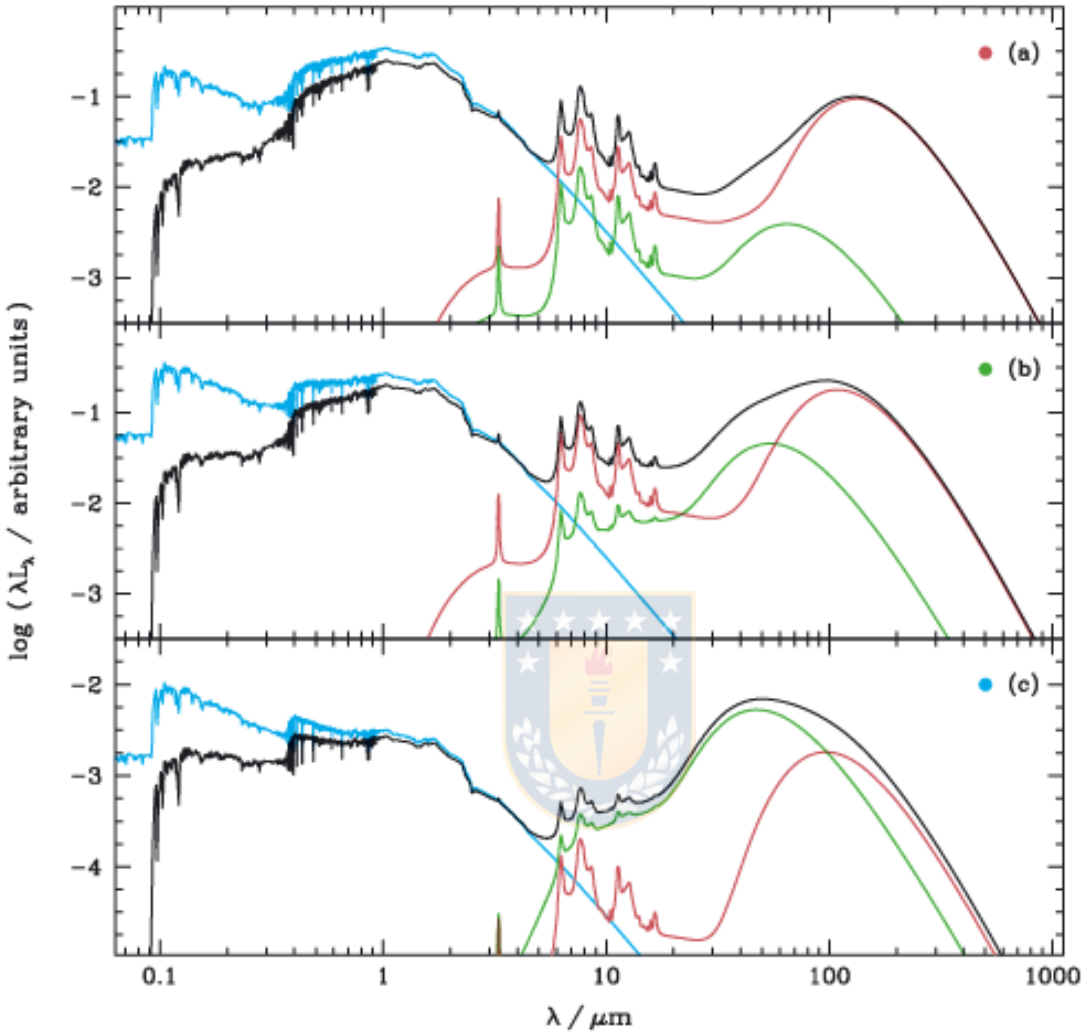

Figura 1.0.11: Examples of Spectral Energy Distributions (SEDs) in galaxies, obtained by combining IR models with attenuated stellar population spectra (da Cunha et al., 2008). These predicts the galactic emission that is absorbed and re-radiated by dust in stellar birth clouds and in the ambient interestellar medium (ISM). The three diagrams correspond to (a) quiescent star-forming galaxy spectrum, (b) normal star-forming galaxy spectrum, (c) SB galaxy spectrum. Each panel shows the unattenuated stellar spectrum (blue line), the emission by dust in stellar birth clouds (green line), the emission by dust in the ambient ISM (red line) and the total emission from the galaxy, corresponding to the sum of the attenuated stellar spectrum and the total IR emission (black line). This model reproduces well the observed SEDs of these galaxies across the entire wavelength range from the far-UV (FUV) to the far-infrared (FIR), and the star formation histories (SFH) and dust contents of the galaxies are well constrained.

Capítulo 2

Sample and Data

Our motivation is to create a large sample of local galaxies which is both well defined and extensively characterized, so as to accurately study the dependence of star formation rates on galaxy mass, i.e. the Main Sequence, in the local universe. In this section we first introduce our sample - the 2MRS-WISE sample - and provide background information on the 2MRS sample and the WISE photometry. We then briefly present complementary photometry and catalogs which are used to test the accuracy and potential biases of our WISE-derived star formation and stellar mass estimates.

2.1. The 2MRS-WISE sample

We use a sample of 40,460 galaxies created by selecting all galaxies in the 2MASS Redshift Survey (Huchra et al., 2012, 2MRS; 43,533 galaxies) for which we could find reliable WISE fluxes at 3.4μm (W1), 4.6μm (W2), and 12μm (W3) in the 2013 version of the AllWISE catalog[1]. From here on we will refer to this sample of 40,460 galaxies as the 2MRS-WISE sample. Note that 1 % of the 2MRS sample (410 galaxies) are lost due to not having WISE fluxes, and the 1750 remaining galaxies (4 % of the 2MRS sample) are lost due to having low signal-to-noise ratios (SNR $\lesssim$ 5) WISE fluxes (see Fig. 2.1.1); our final sample thus retains the overall properties of the 2MRS. We see that from these 410 galaxies without any WISE flux available, 39 correspond to AGNs and 142 to galaxies without an AGN detection (see section 3.6). In addition, from the 1750 galaxies with only low SNRs,

[1]https://irsa.ipac.caltech.edu/Missions/wise.html

58 have are AGNs and 1167 do not have an AGN, with both types having high S/N W4 gmags. A histogram of redshifts of our full 2MRS sample is shown in left panel of Fig. 2.1.1.

The 2MASS Redshift Survey (Huchra et al., 2012, 2MRS; 43,533 galaxies) is a catalog of 43,533 local galaxies (up to $z \sim 0.1$, mean redshift $<z>\sim 0.03$), selected from the Two Micron All-Sky Survey[2] (2MASS, Skrutskie et al., 2006). It effectively provides us with a redshift catalog that is 97.6 % complete to well-defined limits and covers 91 % of the sky (avoiding only the Galactic plane). We note that the 2MASS Extended Source Catalog (2MRS-XSC), while based on images with resolution $\sim 3''$, provides galaxy positions accurate to $0''.5$ for objects with high SNRs ($\gtrsim 5$). The 2MRS catalog provides manually determined morphological types, using a modified Hubble Sequence (de Vaucouleurs, 1963), for a nearly complete sub-sample of 20,869 galaxies at $K_s \leq 11.25$ mag. We also got the radial velocities of the full 2MRS sample, that we convert to luminosity distances by using H_0 =72 km/s/Mpc; for the ∼1,680 galaxies with $V_{recc} < 2005$ km/s we correct V_{recc} (and thus the resulting distance) using the Cosmicflows-3 Distance-Velocity Calculator of the Extragalactic Distance Database [3](CF3, Kourkchi et al., 2020). Further, optical spectroscopy of 26,592 of the 2MRS sample at $z < 0.09$ was used to classify (Zaw et al., 2019) these as either broad-line AGN (1,929), narrow line AGN (3,607 or 6,562 depending on whether the Kewley et al. (2001) or Kauffmann et al. (2003) criteria are used), and galaxies without an AGN detection (18,098 "non-AGN"); emission line fluxes for all these galaxies are also cataloged in Zaw et al. (2019).

The Wide-field Infrared Survey Explorer (WISE) provides all-sky photometry in four MIR bands: 3.4μm, 4.6μm, 12μm, and 22μm (referred to as W1, W2, W3, and W4, respectively) with angular resolutions of $6''.1$, $6''.4$, $6''.5$, and $12''.0$, respectively (Wright et al., 2010). Saturation in WISE images starts to occur when sources are brighter than approximately 8.1, 6.7, 3.8, and −0.4 mag, respectively. We position matched the 2MRS sample of galaxies to the AllWISE Source Catalog, using a maximum radius of $10''$. We got at least one WISE source matched for the 99 % of the 2MRS sources, and thus obtaining W1, W2, and W3 fluxes (specifically, the "g"magnitudes) for almost all of the 2MRS sources. After matching, we proceeded

[2]http://www.ipac.caltech.edu/2mass/
[3]http://edd.ifa.hawaii.edu/

to delete fluxes with low SNRs. Specifically, we deleted W1 to W3 fluxes with wXgerr≥0.2 and W4 fluxes with w4gerr≥0.4, these last being only ∼58.52 % of the full 2MRS sample. Here wXgerr is the magnitude error in WISE-X band, corresponding to SNR∼5. The lower SNR cutoff used for W4 was required since this is the band with the lowest S/N for our sample galaxies; we note that the W4 fluxes are used only to test for consistency with our W3-based SFR estimates. After the SNR cut, we obtained W1, W2, and W3 fluxes for 40,460 galaxies (∼93 % of the 2MRS sources), which then form our 2MRS-WISE sample.

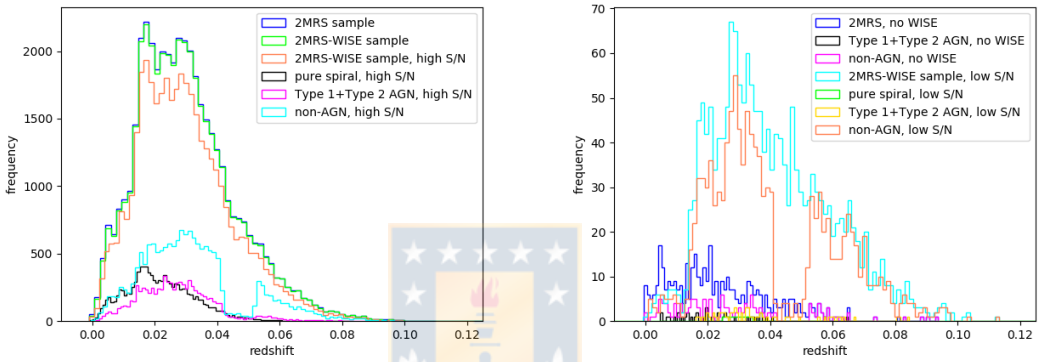

Figura 2.1.1: Left: a histogram of redshifts from the 2MRS-XSC catalog. We count a total of 10,979 pure-spirals with redshifts in our 2MRS-WISE sample, of a total of 43,123 2MRS-WISE redshifts. Right: a histogram of redshifts but only for 1 % of 2MRS sources which do not have any WISE photometry, plus the 2MRS-WISE rejected sources with low SNRs (4 % of the 2MRS sources). See section 3.1 and section 3.6 for the definition of each sub-sample.

2.2. Complementary data

We use several complementary photometry datasets and catalogs to both confirm the accuracy of our WISE-derived stellar masses and star formation rates, and to identify other parameters which could lead to biases in these.

The FIR luminosity provides a highly accurate estimation of SFR in star forming galaxies. We position matched - using a maximum radius of 3′ - our full 2MRS sample with the IRAS Catalog of Point Sources[4](Bei, 1988). Note that this relatively large match radius was used to take into account the relatively low resolution (8′) of the IRAS data; given the brightness and large extents of the low

[4]https://heasarc.gsfc.nasa.gov/W3Browse/iras/iraspsc.html

redshift galaxies in our sample we do not expect many false matches. We thus obtained 60μm and 100μm fluxes for 13,034 galaxies. After deleting IRAS fluxes with errors greater than 20 %, we get a total of 12,809 and 12,608 sources with 60μm and 100μm fluxes, respectively, and a total of 12,396 sources with fluxes in both bands.

We cross matched our full 2MRS sample - using a maximum match radius of 10″ - to the NASA-Sloan Atlas (NSA[5]). For the 16,451 galaxies matched, we thus obtained NUV (1,770-2,730 Å) and FUV (1,350-1,780 Å) fluxes. The NSA is a catalog of 640,000 galaxies at $z < 0.05$, and includes galaxy-wide photometry from data release 11 (DR11) of the Sloan Digital Sky Survey (SDSS, York et al., 2000; Blanton et al., 2011), and the GR6 data release of the Galaxy Evolution Explorer (GALEX, Bianchi et al., 2003; Gil de Paz et al., 2004).

We cross matched our full 2MRS sample - using a maximum match radius of 10″ - to version 2 of the GALEX-SDSS-WISE Legacy Catalog[6] (GSWLC, Salim et al., 2016). The GSWLC (version 2) compiles SDSS, GALEX, and WISE photometry for 659,229 galaxies, plus stellar masses and SFRs derived via a combined fit to this photometry. For the 7,119 galaxies matched, we extracted GSWLC derived values for stellar mass and SFR.

[5]https://www.sdss.org/dr13/manga/manga-target-selection/nsa/
[6]http://pages.iu.edu/ salims/gswlc/

Capítulo 3

Results

3.1. Morphological classification by WISE color

As mentioned in chapter 2, manual morphological classifications, in the modified Hubble scheme, are available for 20,860 galaxies which belong to the 2MRS11.25 catalog (Huchra et al., 2005), plus 5,682 "JH" classified galaxies, thus giving a total of 26,542 morphologically classified galaxies in our full 2MRS sample, and an effective total of 25,908 if we do not count false positives. In this classification, 23 galaxies were classified as QSO/AGNs, 4,445 galaxies as ellipticals (T = −7 to −5), 7,731 as lenticulars (−4 to 0), and 12,754 as spiral galaxies (1 to 9), plus a 955 in other categories (e.g., Irregular, unclassified).

This extensive manual classification allows us to uniquely test the completeness and reliability of previously suggested morphological classifications by WISE colors (Jarrett et al., 2011). Further, since some of the 2MRS morphological classifications are incorrect (given that they used single color optical imaging, rather than the extensive deep multi-band data available today), combining both the manual morphological classifications with morphological classifications based on WISE colors allows us to build a cleaner sample of spiral galaxies.

Previous authors have used the W2−W3 and W1−W2 colors to classify galaxies by morphology as ellipticals, lenticulars, spirals, starbursts, and AGNs (e.g., Jarrett et al., 2011). We want to quantitatively compare the classification based on WISE colors to the manual Hubble sequence classifications in 2MRS, hence, we separate these 2MRS sources in three morphology bins: ellipticals (Hubble type T = −7 to

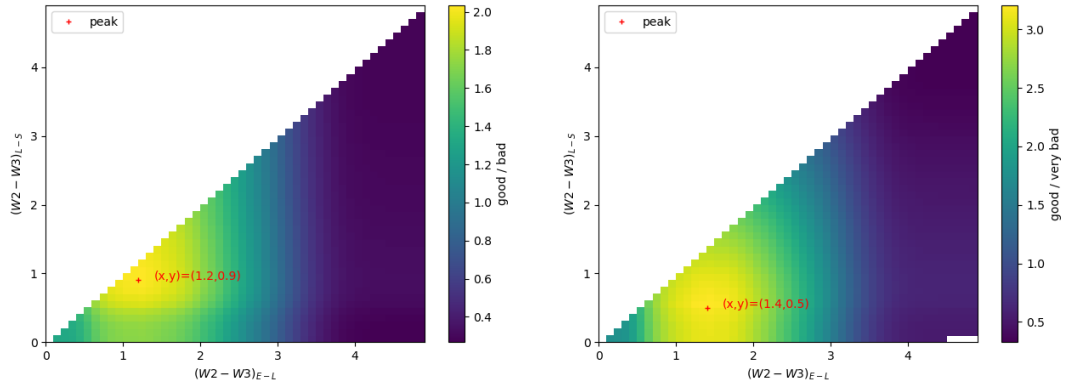

Figura 3.1.1: Concordance between morphological classification from 2MRS (manual) and from WISE W2−W3 color cuts, with larger values showing higher concordance. Left panel: the variation of the ratio g/b (a measure of concordance; see text) as the W2−W3 color cutoff between lenticulars and spirals (x-axis) and that between ellipticals and lenticulars (y-axis) is varied. Right panel: as in the left panel but for the ratio $g/(vb + 0.5b)$ (see text).

−4), lenticulars (T = −3 to 0), and spirals (T = 1 to 9, plus all galaxies listed as unclassified spirals, i.e. T = 20 in the 2MRS tables).

Thus, we compare the elliptical, lenticular, spiral WISE-color classification (for a given two-vector of W2−W3 values to separate these three) to the same elliptical, lenticular, spiral manual classification in a three by three matrix, with elements A_{ij}. We allowed the dividing line between elliptical and lenticulars, $(W2-W3)_{E-L}$ to vary between 0 and 5, and the dividing line between lenticulars and spirals $(W2-W3)_{L-S}$ to vary between $(W2-W3)_{E-L}$ and 5. We count the number of galaxies per each pair of colors $(W2-W3)_{E-L}$ x $(W2-W3)_{L-S}$. Of course, we would like the diagonal values to be high (concordance between the two methods) and the off-diagonal values to be low (disagreement between the two methods). We then create two metrics which reflect the completeness and false positives of the WISE color classification: $ratio1 = g/b$ and $ratio2 = g/(vb + 0.5b)$ where we denominate good data as $g = A_{11}+A_{22}+A_{33}$, bad data as $b = A_{12}+A_{21}+A_{23}+A_{32}$ and very bad data $vb = A_{13} + A_{31}$. That is, the numerator is the sum of the diagonal elements (the concordant classifications) and the denominator considers the off-diagonal elements (non-concordant classifications). In the second metric we give more weight to extremely non-concordant classifications. Plots of these ratios, as the cutoffs $(W2-W3)_{E-L}$ and $(W2-W3)_{L-S}$ are varied, are shown in the two panels of Fig. 3.1.1. For $ratio1$ the best results are obtained for color cuts [0.9, 1.4]

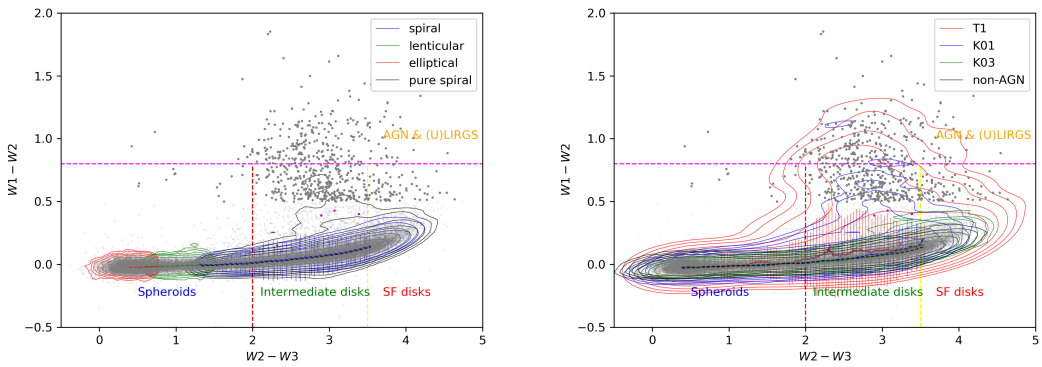

Figura 3.1.2: A WISE color-color diagram of the 2MRS-WISE sample. Left panel: Individual galaxies are shown with grey circles; magenta dots show the 23 Active Galactic Nucleii (AGN) identified by the 2MRS team. We use the color cutoffs from section 3.1 to divide the sample into ellipticals (red contours), lenticulars (green), and spirals (blue). Additionally the "pure-spiral" sample (those classified as spiral by both 2MRS and WISE color; see text) is shown with black contours. All contour maps are normalized to the same scale, i.e., the sum of the ellipticals, lenticulars and spirals, excepting the one for pure-spirals, which has been normalized to the total of pure spirals. Every contour include a running-median (dashed-line) and standard deviation (error bars). Data binning for contours are made using a step size of 0.2 dex. The marginal 0.1 % of the data from colors W1−W2 and W2−W3 and 5 % marginal data in contours have been removed. Right panel: Contours are pure-spirals divided by AGN type, these are Seyfert 1 (red), Seyfert 2 by Kewley et al. (2001) criteria (blue) and Seyfert 2 by Kauffmann et al. (2003) criteria (green), and galaxies which are not AGNs (black). Refer to section 3.6 for further details about our AGN classification. All contour maps are normalized to a different scale, e.g. Seyferts I are normalized by their total of Seyfert I galaxies. Other symbols follow the same rules as in the left panel.

and for *ratio*2 the best results are obtained for color cuts [0.5, 1.2]. These color limits are in relative agreement with the color selections of Mingo et al. (2016), with a W2−W3=1.6 cutoff corresponding to the transition limit between elliptical and spiral morphology (i.e. they do not account for lenticular types).

We suggest using a W2−W3 cutoff of 0.7 to divide ellipticals from lenticulars and 1.4 to divide lenticulars from spirals, but note that even for these "best" values, the completeness of the 2MRS morphology is 40.4 % and false positives is 1.4 %. But note that these are also inflated by some bad classifications in 2MRS. Afterwards, we define the "pure-spirals" in our sample as galaxies which are classified as spirals by *both* the manual 2MRS classification and the WISE colors.

We consolidate the result of our morphological classification in Fig. 3.1.2, that

shows the WISE color-color relation for our 2MRS-WISE galaxies. Red, green, and blue contours with their respective running-medians (dashed-lines) and standard deviations (bars) show where our ellipticals, lenticulars, and (all) spirals fall in the color-color plane. The black contour shows the pure-spiral sample sample which is used to derive the MS in further sections. With increasing W2−W3, W1−W2 remains at ∼0 for values of W2−W3 of 0-2.5, after which it increases both in the median and shows high W1−W2 outliers. Comparing our sample to those already in the literature, e.g., Jarrett et al. (2011); Cluver et al. (2014, 2017), we observe a general agreement. Note that, as expected, our local sample does not include many powerful AGNs (QSO-like) or extreme SBs (i.e. ULIRGs). The latter are expected to have redder colors due to their dusty composition, i.e., higher W2−W3 colors and to have low or quenched SF, which is evidenced by their W1−W2 color. From both panels of Fig. 3.1.2, we see that AGN/(U)LIRGs can be easily distinguished by the limit at W1−W2=0.5, which agrees with the AGN/QSO color cuts made by Mingo et al. (2016), Marleau et al. (2017), also with results plotted in Fig. 1 of Ezhikode et al. (2017) who study a sample of broad-line AGNs. We refer the reader to section 3.6 for a further description of the right panel of Fig. 3.1.2 related to our 2MRS AGN classification.

We conclude this section by making comparisons between sources already classified by 2MRS and WISE morphology in Appendix C, showing that 2MRS classification is in general not reliable, so we give motives to use a WISE morphology instead.

3.2. Stellar Mass

In this section we explain our method to calculate stellar masses, based on mass-to-light ratios from the calibrations of Cluver et al. (2014), expressions that depend on measurements of the in-band WISE luminosities and colors. Afterwards, we compare our set of stellar masses to those derived by Chang et al. (2015) and Salim et al. (2016).

Cluver et al. (2014) used a sample of $z < 0.15$ galaxies to present three potential equations to derive stellar masses from WISE photometry: their eq. 1 come from best fits to sub-samples of resolved galaxies, eq. 2 takes all galaxies in their sample, while their eq. 3 only comes from star-forming (W2−W3 > 1.5) galaxies. The differences between their samples based on eq. 2 and 3 is negligible, and the same

happens when we compare these to our 2MRS-WISE sample, but stellar masses obtained from their eq. 1 are systematically ∼0.18 dex lower than our sample (and up to 0.5 dex lower for a small fraction).

While most of our sample galaxies are resolved in W1 and W2 images (typically 10-30″, and up to 180″), since we cover a large range of W2−W3 colors, and the relations in eq. 2 and 3 of Cluver et al. (2014) are formed from a larger statistical sample of high SNR data, we use their eq. 2 (i.e., all galaxies), which is reproduced below as equation 3.2.1.

$$\log(M_\star/L_{\rm W1}) = -1.96(W1 - W2) - 0.03 \tag{3.2.1}$$

Following to Jarrett et al. (2017), we place ceiling limits on the W1−W2 color in eq. 3.2.1: −0.2 to 0.6 mag, to minimize the contaminating effects of AGN light on our stellar mass estimations.

The W1 luminosities were calculated with the following expression:

$$\mathrm{L_{W1}(L_\odot)} = 10^{-0.4(\mathrm{W1}-3.24)} \tag{3.2.2}$$

Using eq. 3.2.1 and our high S/N W1 and W2 g-magnitudes, we obtain a total of 40,460 stellar masses, spanning the range of $\sim 10^7$-$10^{12}\mathrm{M}_\odot$, with median stellar mass of $10^{10.92}\mathrm{M}_\odot$.

We compare our WISE-derived stellar masses with those from the compilation of Chang et al. (2015) and the GSWLC (Salim et al., 2016). Chang et al. (2015) derived stellar masses and SFRs by applying the MAGPHYS (da Cunha et al., 2012) package to SDSS and WISE photometry of ∼850,000 local galaxies. A comparison of our WISE stellar masses to theirs is shown in Fig. 3.2.1. Galaxies in common to our samples (7,606) cover almost the full range of our stellar masses. We find a very tight 1:1 relationship - within 0.3 dex - for the ellipticals and lenticulars of our sample. However, 20 % of the spirals show disagreement with the 1:1 line of > 0.3 dex: these are mainly spirals classified as Seyfert galaxies (primarily type 1s, with some type 2s). We refer the reader to section 3.6 for further details about the AGN classification used in this work related to Seyfert galaxies.

An equivalent comparison of our stellar masses of those from the GSWL catalog (Salim et al., 2016) is shown in Fig. 3.2.2. With 6,673 galaxies common to both studies, we can only test a smaller dynamic range in stellar mass: early-type galaxies (ETGs) show a small systematic difference (in slope, rather than offset) and some late-type galaxies (LTGs) once more have higher masses in GSWLC. Nevertheless, for 90 % of the galaxies both stellar masses are within 0.3 dex, and once more the outliers beyond 0.3 dex are dominated by Seyfert galaxies.

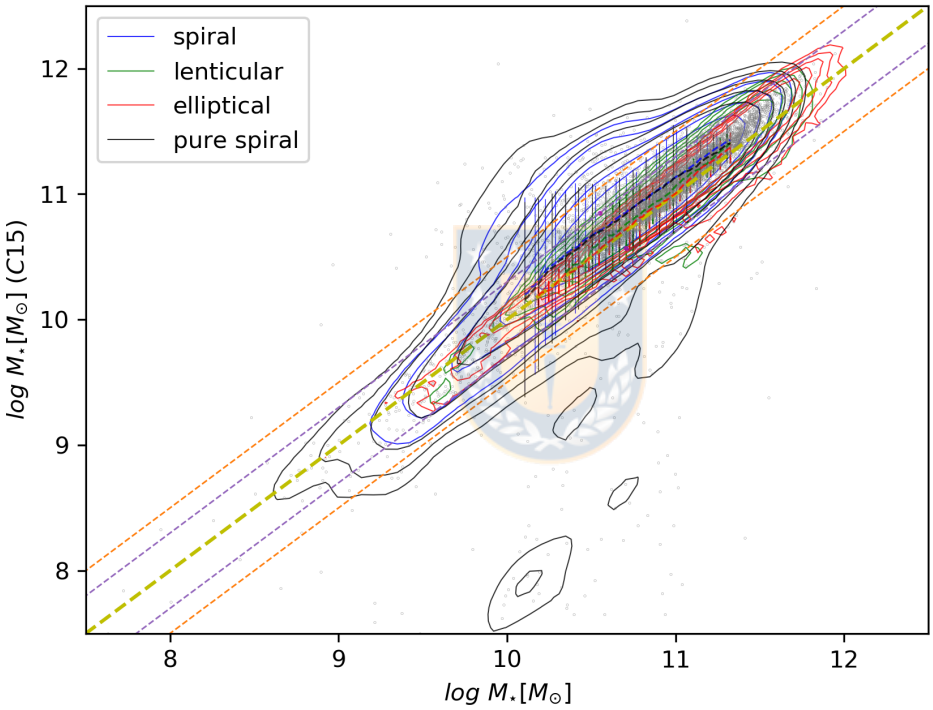

Figura 3.2.1: Comparison of our WISE-derived stellar mass to those from the Chang et al. (2015) compilation. Contour colors are used to differentiate morphologies following Fig. 3.1.2 and the inset. Data points are shown with gray open circles and for each set of contours, the median is plotted with a dotted line of the same color. The line of equality is shown in yellow. We illustrate limits for the AGN population contaminating our sample (bump over the upper limits) that has not been disentangled from the normal star-forming galaxies in our sample, by an orange dashed-line of ±0.5 dex, and a purple dashed-line of ±0.3 dex, which delineates the limits of the running-median for these normal star-forming galaxies.

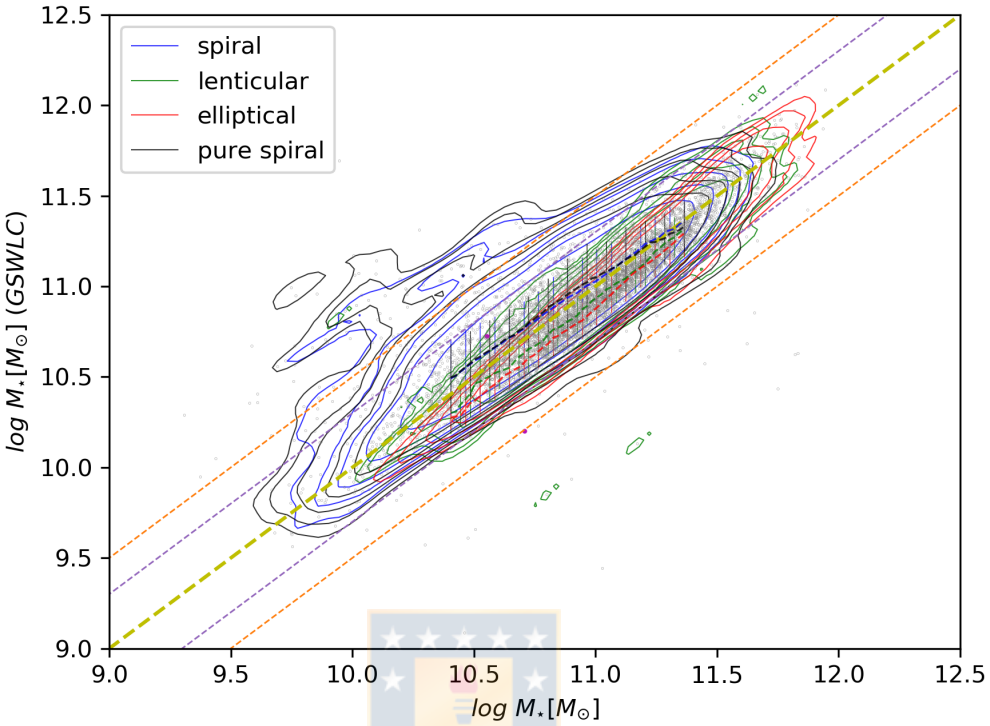

Figura 3.2.2: As in Fig. 3.2.1 but this time comparing our WISE-derived stellar mass with those from the GSWL catalog of Salim et al. (2016).

3.3. Star Formation Rates

In this section we derive SFRs for the sample galaxies using WISE W3 band fluxes: obtaining SFRs for a total of 40,460 galaxies. For W4, roughly half of the sample have available SFRs, having lower SNRs.

We use the relationships of Cluver et al. (2017) to estimate SFRs from WISE-3 (W3; 12μm) and WISE-4 (W4; 23μm) bands: these were derived using 79 SINGS/KINGFISH galaxies, which include 33 ($\sim$41 %) AGNs and (U)LIRGS. Total IR luminosities (L_{TIR}) are estimated from luminosity densities in the 12μm ($L_{12\mu m}$) and 23μm ($L_{23\mu m}$) bands as follows:

$$\log L_{TIR}(L_\odot) = (0.889 \pm 0.018) \log L_{12\mu m}(L_\odot) + (2.21 \pm 0.15) \quad (3.3.1)$$

$$\log L_{TIR}(L_\odot) = (0.915 \pm 0.023) \log L_{23\mu m}(L_\odot) + (1.96 \pm 0.20) \quad (3.3.2)$$

This is then converted to an SFR using eq. 3 of Cluver et al. (2017), which is

effectively eq. 1.3 of Calzetti (2013), which assumes a Kroupa IMF:

$$\mathrm{SFR}\ (\mathrm{M}_\odot\ \mathrm{yr}^{-1}) = 2.8 \times 10^{-44}\ \mathrm{L_{TIR}}\ (\mathrm{erg/s}) \tag{3.3.3}$$

This relationship provides us with SFRs from W3 and W4 bands spanning from $\sim 10^{-3}$-$10^{3}\mathrm{M}_\odot\ \mathrm{yr}^{-1}$. By looking at Fig. 3, panel a of Cluver et al. (2017), we see a tight relationship between $\mathrm{L_{TIR}}$ and $\mathrm{L}_{12\mu\mathrm{m}}$ luminosities for normal star-forming galaxies, whilst the relationship shown in panel b of $\mathrm{L_{TIR}}$-$\mathrm{L}_{23\mu\mathrm{m}}$ exhibits the same trend than panel a, but with larger scatter, with such difference becoming more clear at intermediate luminosities (i.e., $\sim 10^{8}$-$10^{10}\ \mathrm{L}_\odot$). Cluver et al. (2017) show that W3 luminosities in galaxies have a more constant than W4 luminosities when compared to their total IR luminosities. Besides, they probed that W3 is better tracer of SFR than W4 in normal star-forming galaxies. Therefore, from the ideas presented here we determine that our for sample of 2MRS-WISE galaxies W3 is a better proxy of SFR than W4.

Then, in order to test the reliability of our W4 SFRs, we want to determine the offset between our W3-based SFRs and W4-based SFRs. This comparison is shown in Fig. 3.3.1. Here, we see that top and bottom diagrams correspond to our 2MRS-WISE galaxies classified by morphology and AGN type, respectively, following our classifications from sections 3.1 and 3.6. In both panels, the set of data points (grey circles and its contours) exhibits a turnover towards high SFRs, at the limit of $\sim 10\ \mathrm{M}_\odot\ \mathrm{yr}^{-1}$, and for SFRs approaching the $\sim 1\ \mathrm{M}_\odot\ \mathrm{yr}^{-1}$, whilst in the bottom panel we such a turnover in the highest SFRs corresponds mostly to the T1 (Type 1 AGN) population. In general, running-medians (thin black dashed-lines) are in agreement within the 0.2 dex offset from the expected line of equality (yellow dashed-line), in both, pure-spiral galaxies (left panel) and non-AGN sources (right panel). Furthermore, we see a tight correlation between running-medians, contours and the expected line of equality for the pure-spirals.

We also show a similar relationship to that given by eq. 8 from Cluver et al. (2017). This best-fit to our full sample of W3 and W4 SFRs is denoted by a (thick) black dashed-line, which corresponds to a best-fit to the W3 and W4 SFRs in our full pure-spiral sample, that has the following form:

$$\log \mathrm{SFR_{W4}}/[\mathrm{M}_\odot/\mathrm{yr}] = 1.08 \log \mathrm{SFR_{W3}}/[\mathrm{M}_\odot/\mathrm{yr}] - 0.14 \tag{3.3.4}$$

By comparing this equation to the one characterizing the SINGS/KINGFISH sample, we find offsets spanning between ∼0.08 to 0.15 based on the upper/lower errors associated to slopes in eq. 8 from Cluver et al. (2017). Also we find offsets spanning between ∼0.12 to 0.14 based on the errors in the intercept.

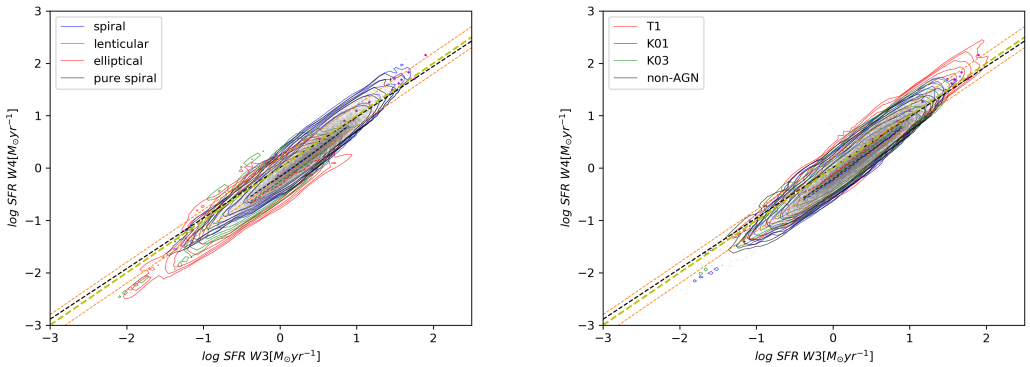

Figura 3.3.1: Comparison between W3 and W4 SFRs. A yellow dashed-line is the expected line of equality. A linear best-fit have been performed for the pure-spiral sample (thick black dashed-line). An orange dashed-line is the 0.2 dex offset from the line of equality. The left and right panels follow the classification used in Fig. 3.1.2, i.e., by morphology and by AGN type, respectively.

Similarly, in Fig. 3.3.2 we show the ratio of W3 and W4 SFRs as a function of stellar mass. We see that ETGs have systematically higher W3 SFRs (by about 0.3 dex) while LTGs show a trend of W3 SFRs increasing over W4 SFRs as stellar mass increases, reaching a systematic median difference of 0.2 dex at the highest stellar masses.

Once we have calculated SFRs for our full sample of 2MRS-WISE galaxies, as a consistency check we compare our W3-based SFRs to other SFR tracers from the UV, IR, and UV+IR available in literature. We show the results of these comparisons in Fig. 3.3.3, whilst the equations used for these comparisons are detailed in appendix A.

First, we estimate the ratio of SFR_{WISE} and SFR_{GSWLC} (left upper panel) as a function of stellar mass, where we see that SFRs from pure-spirals (black contours) are within a ∼1 dex scatter. Such a big dispersion starts at ∼0.3 dex and scales up to ∼0.5 dex when approaching the limit of $\sim 10^{10.5} M_\odot$, keeping it roughly constant along the whole range of masses. In the case of lenticular and elliptical galaxies, we see very high SFRs in the W3 band, with up to a 3 dex median offset with respect to the GSWLC sample of galaxies from Salim et al. (2016). These

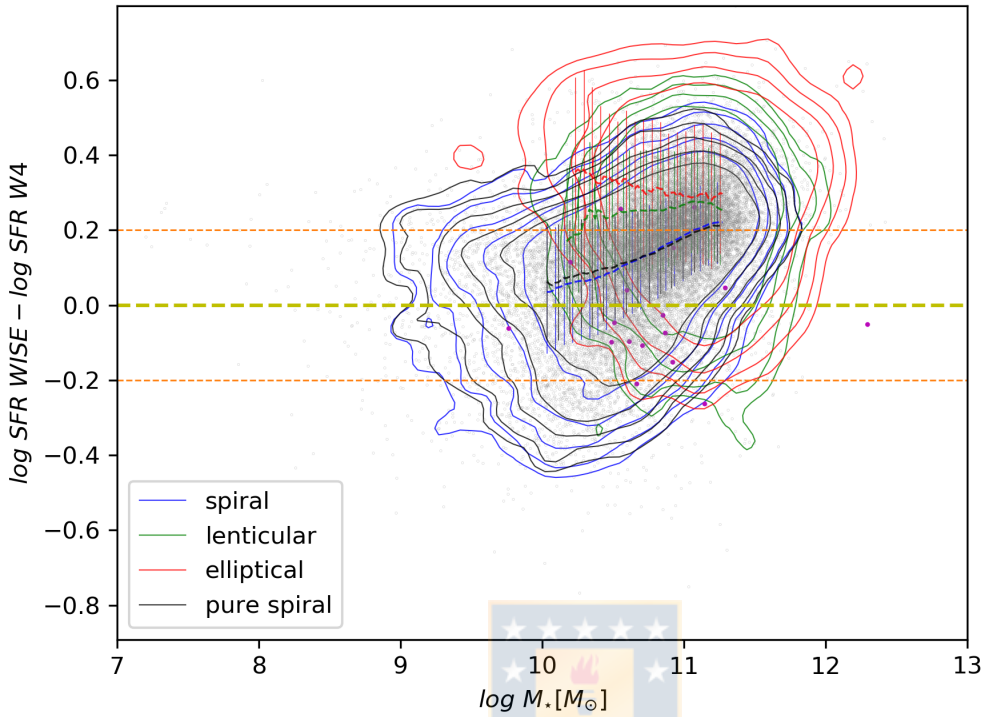

Figura 3.3.2: The difference between W3- and W4-based (log) SFRs for our sample galaxies as a function of our WISE-derived stellar mass. Red, green, blue and black contours are used for ellipticals, lenticulars, spirals and the pure-spiral sample, following the inset. Running-median values (dashed-lines) and standard deviations (bars) are displayed for each sub-sample. Grey circles are WISE-2MRS galaxies and magenta dots correspond to 2MRS galaxies classified as AGNs by Huchra et al. (2012). Units of the y axis are $M_\odot$ yr^{-1}.

ellipticals show the lowest SFRs, whilst pure-spiral galaxies hold the relation of equality (yellow thick dashed-line is the expected relation of equality) within the 0.5 dex. In the case of ETG sources, the larger median offset is likely a consequence of LTG starlight lost due to strong obscuration by dust at shorter wavelengths, where the total UV-optical light can not be compensated by IR measurements. Therefore, we conclude that our MIR dust-based SFRs from W3 band follow the relation of the GSWLC galaxies with maximum median offset ∼0.5 dex, so we have that our sample of pure spirals are constrained in their optical-UV SFRs by MIR observations of the WISE bands. On the other hand, from Fig. 3.3.3 we see that for our NUV, FUV and total IR SFRs the equality relation (yellow dashed-line) is held within ∼0.2 dex (orange dashed-lines) and a deviation comparable to this

quantity.

In general, we have that W3 SFRs have a roughly constant behaviour when compared to other SFRs (as expected from results of Cluver et al., 2017), whilst in the case of W4 SFRs, the results are the opposite, (not shown in this work, but see Fig. 3.3.2) with W4 decreasing monotonically with increasing stellar masses from ∼0.2-0 dex median offset, when compared to the literature presented here. Such a decrease occurs in both, normal star-forming galaxies and AGNs in our sample of W4 SFRs, although it still roughly constant in W3 band. Thus, this fact argues again in favour of W3, which has a more constant response than W4 when compared to other SF tracers.

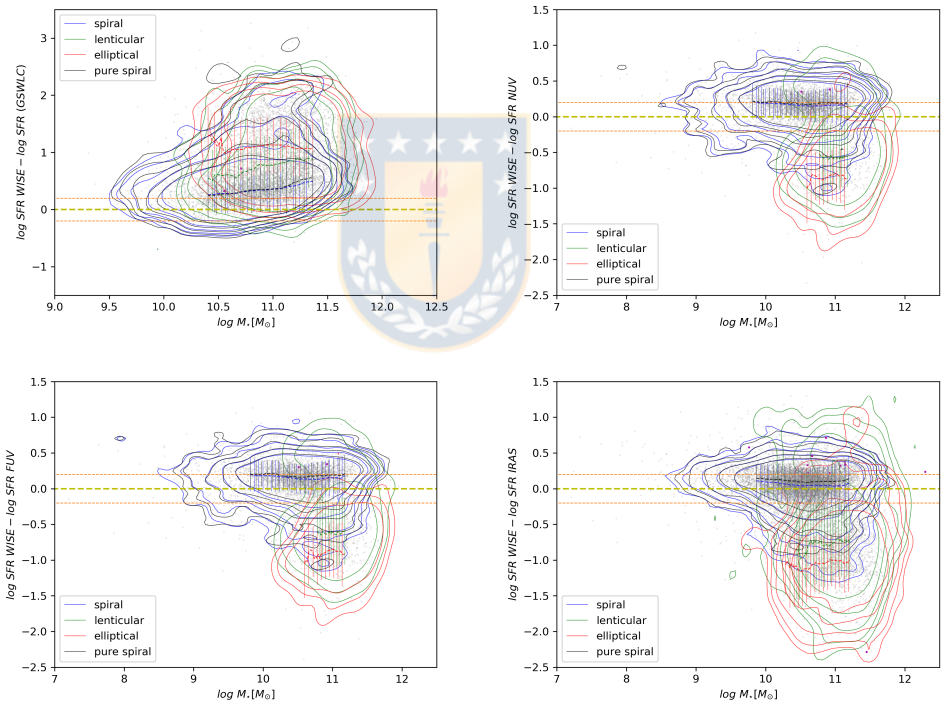

Figura 3.3.3: A comparison of different SF indicators to the WISE W3 SFR indicator, where we use eq. 3.3.3 as a function of stellar mass.

Therefore, by results obtained in this section and for a matter of consistency among the different SF tracers used in this work, we must add an offset of ∼0.2 dex to each SFR derived along this work as a measure of the uncertainty between W3/W4 and other bands. This uncertainty must be added to every SFRs calculated in this section, thus, affecting to our MS results (intercept) that are described in the next section (3.4).

Summarizing the previous ideas discussed in this section: for our 2MRS-WISE sample, we have made comparisons between W3 and W4 SFRs, determining a maximum median offset of ∼0.15 in slope and intercept between these two quantities. We also have determined a roughly constant median offset of ∼0.2 dex between our W3 derived SFRs and those SFRs from other bands. The same offset appears in W4 SFRs when compared to the same set of SF tracers, including W3, but note that W4 does not show a constant offset; unlike W3, W4 is rather is decreasing with increasing stellar masses. In particular, these median offsets are observed in SFRs from total IR and IR-calibrated UV sources. Thus, we find that all of our results argue that the W3 band is a more reliable tracer of SF than W4, which motivate us to use it as our main tracer of SF in the construction of a MS. Therefore, we determine that our SFRs calculated in this section must have corrected by a ∼0.2 dex offset for consistency between the different SF tracers.

3.4. z=0 Main Sequence and its dispersion

In this section determine the characteristics of the z∼0 MS based on our 2MRS-WISE sample, and using our W3 SFRs (equation 3.3.3). Specifically, we characterize the turnover in the MS, the slopes and intercepts of each MS segment, and the intrinsic scatter of the MS.

Fig. 3.4.1 shows the relationship between (our W3-based) SFRs and (WISE-based) stellar masses - the so called Main Sequence of star formation in galaxies. The 2MRS-WISE galaxies are shown with grey circles; magenta circles highlight those classified as AGN by Huchra et al. (2012). The different color contours show the distribution of mophological sub-samples of the 2MRS-WISE sample (section 3.1): pure-spirals (black), spirals (blue), lenticulars (green) and ellipticals (red). For each, we show running-medians (dashed-lines) and standard deviations (as error bars) in the same colors. Clearly, the contours, and running-medians, of both spirals and pure-spirals do not correspond to a single power-law. At log stellar masses lower than ∼10.4, we are in very good agreement with the earlier proposed MS of Elbaz et al. (2011), but there is a clear turnover in the MS at higher stellar masses.

Cuadro 3.4.1: Results of the log-normal Gaussian fits to the pure-spiral galaxies in each stellar mass bin[1]

N_{gal}	$\mu_{M_\star}$ $[M_\odot]$	$\sigma_{M_\star}$	μ_{SFR} $[M_\odot\ yr^{-1}]$	σ_{SFR}	μ_{sSFR} $[yr^{-1}]$	σ_{sSFR}
3	7.25	0.039	-2.47	0.11	-9.64	0.152
4	7.91	0.024	-2.0	0.08	-9.87	0.066
2	8.08	0.025	-1.9	0.45	-9.99	0.42
5	8.31	0.056	-1.92	0.20	-10.21	0.26
7	8.48	0.055	-1.25	0.26	-9.81	0.25
15	8.71	0.064	-1.66	0.15	-10.36	0.18
18	8.91	0.048	-1.32	0.33	-10.23	0.32
47	9.09	0.065	-1.03	0.25	-10.12	0.24
68	9.31	0.055	-0.77	0.21	-10.16	0.21
128	9.5	0.054	-0.6	0.25	-10.09	0.22
222	9.7	0.054	-0.26	0.27	-10.02	0.24
379	9.91	0.053	-0.08	0.31	-10.01	0.27
715	10.11	0.053	0.11	0.32	-9.99	0.32
1186	10.3	0.063	0.29	0.31	-10.05	0.30
1671	10.5	0.065	0.38	0.31	-10.11	0.31
2104	10.7	0.072	0.51	0.31	-10.16	0.31
1957	10.89	0.072	0.51	0.36	-10.38	0.33
1560	11.09	0.061	0.53	0.29	-10.58	0.29
681	11.28	0.046	0.58	0.25	-10.71	0.28
164	11.47	0.044	0.76	0.26	-10.7	0.24
24	11.66	0.038	0.84	0.24	-10.76	0.24
4	11.84	0.008	0.97	0.016	-10.85	0.02

For each stellar mass bin between $10^{8.4}$-$10^{11.8}M_\odot$, in steps of 0.2dex, we fit a Gaussian to the distributions of stellar mass, SFR, and SSFR for galaxies in the bin, and thus obtain the mean and dispersion of the distributions. The fits are shown in Fig. 3.4.3, and the results in Table 3.4.1, and as pink points and their error bars in Fig. 3.4.1. For stellar bins outside this range, there are too few galaxies for a meaningful Gaussian fit, so we use the direct mean and dispersion of the points (see Table 3.4.1).

In Fig. 3.4.3 one can clearly see a tail to high SSFRs (as it has been previously

[1]Note that for each stellar mass bin we list the number of galaxies (N_{gal}), and the mean μ and σ of the Gaussian fit to the stellar mass, SFR, and SSFR. These bins with size 0.2 dex spans between $10^{7.2}$-$10^{7.4}M_\odot$ and $10^{7.8}$-$10^{12}M_\odot$. The first 4 rows and the last row (corresponding to a total of 5 bins) of this table have not been plotted in Fig. 3.4.1, due to their poor statistics (see text).

observed by Rodighiero et al., 2011; Popesso et al., 2019a; Guo et al., 2013; Schreiber et al., 2015) which represent the SB galaxies. At SSFRs lower than the Gaussian fit we also see some extra peaks, which may represent ETGs which were wrongly classified by their WISE colors. In particular, these peaks of SBs start to vanishing from histograms in the limit of $10^{10.2}$-$10^{10.4}$M$_\odot$, which is consistent with the presence of a bending MS (seen) and with the fact that our MS effectively starts to flatten at $10^{10.4}$-$10^{10.6}$M$_\odot$.

The means from the Gaussian fits to the stellar mass and SFRs in each stellar mass bin (pink circles in Fig. 3.4.1) cannot be fitted by a single MS, therefore we use two fits, obtaining a MS (cyan dashed-line) with a clear bending at high stellar masses, and with a range of turnover mass spanning between $10^{10.4}$-$10^{10.6}$M$_\odot$ as pointed out by Whitaker et al. (2014), which is also supported by the apparent turnover seen in contours. This range of turnover is also in good agreement with the results of Schreiber et al. (2015); Popesso et al. (2019a), and concordant with the green line in Fig. 3.4.3 (MS prediction from Elbaz et al., 2011). Such a turnover separates the MS in two different power-laws, one low mass end for stellar masses lower than $10^{10.4}$M$_\odot$, containing 2,801 low mass pure-spirals, and a high mass end, for masses higher or equal to $10^{10.4}$M$_\odot$, which contains over 8,177 high mass pure-spirals. In general, we see that the low mass end of our MS posses larger scatter than the high mass end. From the best-fit to our MS, we determined a low mass slope of $\sim$1.05 that is in good agreement with the single power-law MS prediction from Elbaz et al. (2011); we also determined an intercept of ~ -10.56. The dispersion of this low mass MS corresponds to a mean quadratic error of 0.03 and statistical error of 0.94. The equation that describes our broken power-law MS in this case has the form:

$$\log \mathrm{SFR}_{\mathrm{low,MS}}/[\mathrm{M}_\odot/\mathrm{yr}] = 1.05 \log \mathrm{M}_\star/[\mathrm{M}_\odot] - 10.56 + \mathrm{C}_{\mathrm{off}} \tag{3.4.1}$$

which assumes values between 0 to -0.2 dex, that is indicative of the $\sim$0.2 dex uncertainty in our SFRs, relative to the offset determined in section 3.3. We also determined a bending of the high mass MS that is in good agreement with the displayed average (mean) values and standard deviations in the center of the contour maps of our pure-spiral sample. From the linear best-fit we got a slope of $\sim$0.36 and intercept ~ -3.43 for the high mass MS, with a mean quadratic error of 0.0 and statistical error of 0.89. Such a high mass slope is in good agreement with

results of Popesso et al. (2019a). Thus, the equation that describes our broken power-law MS at the high mass regime has the form:

$$\log \mathrm{SFR}_{\mathrm{high,MS}}/[\mathrm{M}_{\odot}/\mathrm{yr}] = 0.36 \log \mathrm{M}_{\star}/[\mathrm{M}_{\odot}] - 3.43 + \mathrm{C}_{\mathrm{off}} \tag{3.4.2}$$

where C_{off} is an offset which is already explained in the text from above.

If we use W4 band instead of W3, we obtain a similar MS. This result can be checked in appendix B.

In Fig. 3.4.2 we plot the SFP of nearby galaxies but using a set of stellar masses and SFRs from the GSWL Catalog of Salim et al. (2016), whose limits of stellar mass are $\sim 10^{8.52}$-$10^{12.11}\mathrm{M}_{\odot}$. Our derived MS based on W3 SFRs (cyan dashed-line) is included for comparison. This version of the SF plane shows galaxies from the GSWLC sample which have been cross-matched to our 2MRS-WISE galaxies, where we see, for example, the GSWLC galaxies classified as pure-spirals (black contours) and their running-medians (black dashed-lines). These roughly constant running-medians shows a significant offset between the GSWLC and those from our MS within ∼0.5 dex, mostly representing lower SFRs of 1 $\mathrm{M}_{\odot}$ yr^{-1}, whilst standard deviations (black bars) of the GSWLC pure-spirals are ∼0.5 dex and therefore we see that our MS (and its running-medians) agrees within a certain level. However, although we applied the same WISE classification to the GSWLC sample, it still looks highly biased in comparison to our clean 2MRS-WISE sample.

Therefore, summarizing our MS results from this section: we have determined that it is well described by a broken power-law with a clear bending at the high mass end. We also determined an intrinsic scatter of this MS spanning between 0.15-0.36 dex, which do not monotonically increase with stellar mass, and a turnover mass within the range of $10^{10.4}$-$10^{10.6}\mathrm{M}_{\odot}$, which separates the MS in two power-laws, one low mass MS with slope ∼1.05 and high mass MS of slope ∼0.36.

3.5. Main Sequence evolution with redshift

We test completeness of our pure-spiral sample over the local redshift $z \leq 0.03$. In Fig. 3.5.1 we plot our derived SSFRs as a function of redshift, where data is described by grey circles. We highlight our full pure-spiral sample with black contours, which spans in a wide range of SF levels, whose running-medians (black

dashed-line) decrease with increasing redshift and show standard deviations within ∼0.5 dex in average (vertical bars) along the median range of redshift considered. The black contours have been normalized by the total of pure-spirals. We see a roughly linear (logarithmic scale), monotonic decrement of median SSFRs towards higher redshifts, with running-medians spanning from $\sim 10^{-10.2}$ yr^{-1} to $\sim 10^{-10.5}$ yr^{-1}, between z∼0.02 and z∼0.04. The mean and median SSFR of our full set of pure-spirals is $\sim 10^{-10.26}$ yr^{-1}.

We determine that a decreasing SSFR with look-back time is uncertain due to the unknown fraction of AGN at the lower redshifts in our sample, plus the fact that the sample of pure-spiral galaxies in question has not been disentangled from the SB populations, that are expected to lie at the uppermost part of the diagram.

3.6. The role of AGNs

In this section we want to perform a good classification of our pure-spiral sample by their AGN content, aiming to clean-up our MS galaxies from any AGN contamination. In the following, we want to define an AGN sample and to characterize it by establishing relations of total IR luminosity, bolometric luminosity and overall SF in a given galaxy.

Here we distinguish between two classes of galaxies: AGNs, that are both normal star-forming and have an active nucleus, and those normal star-forming that lack of active nucleus, which we denote as non-AGNs. The former must have a well-resolved dusty torus with accreting gas flows in the innermost central parts, which can be well defined or not, depending on if they have a face-on disk, or well, an edge-on galactic disk (Antonucci, 1993; Dumas et al., 2007, and references therein). SF from the central parts of a given galaxy may result affected by the brightness of an outflow while its nucleus remains active, although it is expected to be a negligible contribution to the overall SF (Jarrett et al., 2013; Popesso et al., 2019b).

Our AGN data set is a sub-sample of the 2MRS-XSC, which were classified as AGN by Zaw et al. (2019): their published catalog contains type 1 (T1), type 2 (K01) by the Kewley et al. (2001) criteria or type 2 (K03) by Kauffmann et al. (2003) criteria. Zaw et al. (2019) list a 2MRS data set with 26,591 objects, from which 8,494 galaxies are AGNs and 18,098 were classified as non-AGNs galaxies.

From this sample, we asses a total sub-sample of 16,458 non-AGN and 8,274 AGN with high SNRs (i.e. wXgerr<0.2), of which 1,883 galaxies are classified by AGN type as T1, 3,522 as K01 and 2,869 are K03. Further, from these high S/N AGN and non-AGN, we count the overall number of spiral galaxies, determining: 855 T1, 1,176 K01, 1,273 K03 and 3,841 non-AGNs. Similarly, we assess the total of pure-spirals with high SNRs, that hereafter we refer to as our AGN sample: 827 T1, 1,026 K01, 1,229 K03 and 3,098 non-AGNs, therefore, 37,353 2MRS galaxies were not classified by AGN content, giving a total of 3,082 (7 % of our full 2MRS sample) AGNs which are both high SNR and pure-spirals.

Firstly, we want to characterize our full AGN sample by their total energy budget arising from traces of ionized gas emission, which is a common tracer of AGN radiation; this is then compared to the overall IR luminosity from the harbouring galaxy. Thus, we aim to find out how AGN bolometric luminosity becomes the dominant output and on which type of galaxy this happens, establishing a link between their total IR luminosity and AGN bolometric luminosity. For this purpose, we proceed to compare AGN bolometric luminosities ($L_{bol,OIII}$) to total IR luminosities (L_{TIR}), using the expression from Heckman et al. (2004) to calculate bolometric luminosities from the OIII line, that has the form $L_{bol} = 3500 \times L_{OIII}$ whilst the total IR luminosities were already calculated in section 3.3 using eq. 3.3.1.

The comparison between total IR luminosities and AGN bolometric luminosities is shown in Fig. 3.6.1, where we see that our total IR luminosities spans between $\sim 10^{42}$-10^{45} erg/s and have roughly constant running-medians with values close to $\sim 10^{44}$ erg/s (mean and median $\sim 10^{43.9}$erg/s). The diagram tells us that there is a few orders of magnitude between our set of IR luminosities and $L_{bol,OIII}$ (see the yellow dashed-line of equality), the latter with common or median values representative of both, non-AGN sources (mean and median $\sim 10^{41.9}$ erg/s) and AGN 2s (mean and median $\sim 10^{42}$ erg/s). The range of bolometric luminosities in our sample spans between $\sim 10^{39}$-10^{46} erg/s (mean and median $\sim 10^{42}$ erg/s), which is roughly the range of the set of radio quiet AGNs from Mingo et al. (2016), although there is a significant difference between the range of redshift considered. If we compare our range of bolometric luminosities to the sample used by Audibert et al. (2017), who studied AGN 1s and 2s at redshift 0.002-0.007 (which is in agreement with results from Oh et al., 2015), their lowest limit of luminosity is

higher than ours by ∼3 orders of magnitude, but coincide in the peak of luminosity. This difference between both limits places our sample of broad-line and narrow-line AGN bolometric luminosities below those from Audibert et al. (2017) in average by two orders of magnitude. Further, we see a few type 1 (Seyfert I, mean and median $\sim 10^{42.5}$ erg/s) and type 2 (K01, Seyfert II; mean and median $\sim 10^{42.1}$ erg/s) AGN that exhibit the highest AGN bolometric luminosities, peaking at the range of $\sim 10^{44}$-10^{46} erg s^{-1}, which is shown by the most extreme contours. This range of AGN bolometric luminosities exceeds by 1-2 orders of magnitude the L_{TIR}, which is a characteristic of QSOs. Therefore, we have that our estimations of bolometric luminosity are not in general equal to the total IR output in a given galaxy, but such an equality is only seen in the most powerful type 1 and type 2 AGN.

Now we want to determine how the peak of AGN bolometric luminosity is related to the overall SF in galaxies, and if it implies a significant increase of their SSFRs. Then, we plot SSFRs (mean and median $\sim 10^{-10.28}$ yr^{-1}) versus AGN bolometric luminosity in Fig. 3.6.2, where we see that Type 1 (T1, mean and median $\sim 10^{-10}$ yr^{-1}) and type 2 (K01, mean and median $\sim 10^{10.5}$ yr^{-1}) AGNs in general have increasing SSFRs with increasing bolometric luminosities. We also see that a peak of SSFRs is reached mostly by type 1 AGN, being roughly $\sim 10^{-8.7}$ yr^{-1} at a peak luminosity of $\sim 10^{44}$-10^{45} erg/s, as shown by the most extreme contours. These more actively star-forming AGN extend their bolometric luminosities from $\sim 10^{44}$ to 10^{46} erg/s. At lower AGN luminosities or lower SSFRs, K01 AGNs and non-AGNs (mean and median $\sim 10^{-10.3}$ yr^{-1}) have in average relatively low values of SSFR, values commonly found in elliptical galaxies.

We check consistency between the SSFRs already seen in Fig. 3.6.2 and the SFP derived in section 3.4. For this we plot the AGN version of our SFP in Fig. 3.6.3, where we find that pure-spiral galaxies show trends that are similar to those of non-AGN galaxies and type 2 AGN (K03), along the whole stellar mass range. In particular, we see a lack of AGN sources at the lowest stellar masses. However, the most interesting feature is that data and contours from the most starbursty AGNs coincide with the excess seen in SB galaxies, which is clearly shown by red contours, representative of Seyfert I and II (K01) galaxies. Therefore, this MS support the peak of SSFRs observed in previous Fig. from this section, that is mainly seen in type 1 AGN.

Therefore, from results obtained in this section we conclude that our MS is biased

mainly by type 1 AGN and type 2 (K01), which should correspond to the SB galaxies included in our pure-spiral sample, so we can infer that our MS of galaxies is not being significantly contaminated by AGNs.

Having our AGN sample characterized, we discuss our results from the right panel of Fig. 3.1.2, in section 3.1. In such a diagram we present our full 2MRS-WISE sample which has been classified by AGN content in this section. The resulting WISE color-color diagram strongly supports the idea that our AGN sample is obiquitous, and that these can be easily identified by their W1−W2 colors higher than ∼0.5 (mostly T1 and K01 AGNs) and W2−W3 colors higher than ∼1.5, so its a good start to think that our pure-spiral sample towards higher W1−W2 colors is a population of combined AGN/(U)LIRGs. We see that WISE galaxies start to show clear AGN features at W1−W2∼0.2 colors and becoming well defined above the limit of W1−W2∼0.4, therefore having general agreement with the WISE color diagram in Fig. 21 of Mingo et al. (2016). We have that most of type 1 and type 2 (K03) AGNs spans in a wide range of colors, whilst type 2 AGNs (K03) seem to be mostly LINERs that falls below the W1−W2∼0.4 limit. In general, the low density of data points within the contour maps allow us to clearly differentiate Seyfert galaxies from spiral galaxy populations.

Finally, we asses that SB galaxies are relatively few in comparison to the total of MS galaxies plotted in Fig. 3.4.1, this fact is supported by our SFP based on an AGN classification (from this section) and by conclusions from further sections 3.7 and 3.8. These SBs span within a smaller range of colors than those from Jarrett et al. (2011), where we noted that highly star-forming AGNs are mostly broad-line (T1, red contours) and narrow-line (K01, blue contours), as have been argued in previous lines of this section.

3.7. The most massive galaxies in the MS

From our set of MS galaxies, we count a total of 2 SBs in a total of 150 most massive galaxies, by visually checking their DR15[2] images and spectra, hence, we conclude that SB contribution to the overall SF in the W3 MS is expected to be negligible for the most massive galaxies. This is supported by our results of section 3.3 and Fig. 3.4.1, where we assess the same conclusion.

[2]http://skyserver.sdss.org/dr15/en/tools/chart/list.aspx

3.8. The most extreme starbursts: low mass end and high mass end

By using a similar method to that from the previous section 3.7, we count a total of only 1 SB spectrum from a total of 150 most starbursty galaxies in the high mass end of the MS derived in this work. Whilst for the low mass end, from a total of 150 galaxies, we found 2 SBs, one of them corresponding to a merger pair. These two sets of 150 galaxies were also visually confirmed by using the SDSS DR15 online tool. Thus, we asses a total of 1 SB galaxy in both, low and high mass end. Therefore, contribution of SBs to the MS is expected to be negligible for the most starbursty galaxies in both range of stellar masses.

From results obtained in these sub-sections, we conclude that the observed SB population is negligibly contributing to the total number of MS galaxies, therefore, contamination of our MS by SBs must be considered negligible.

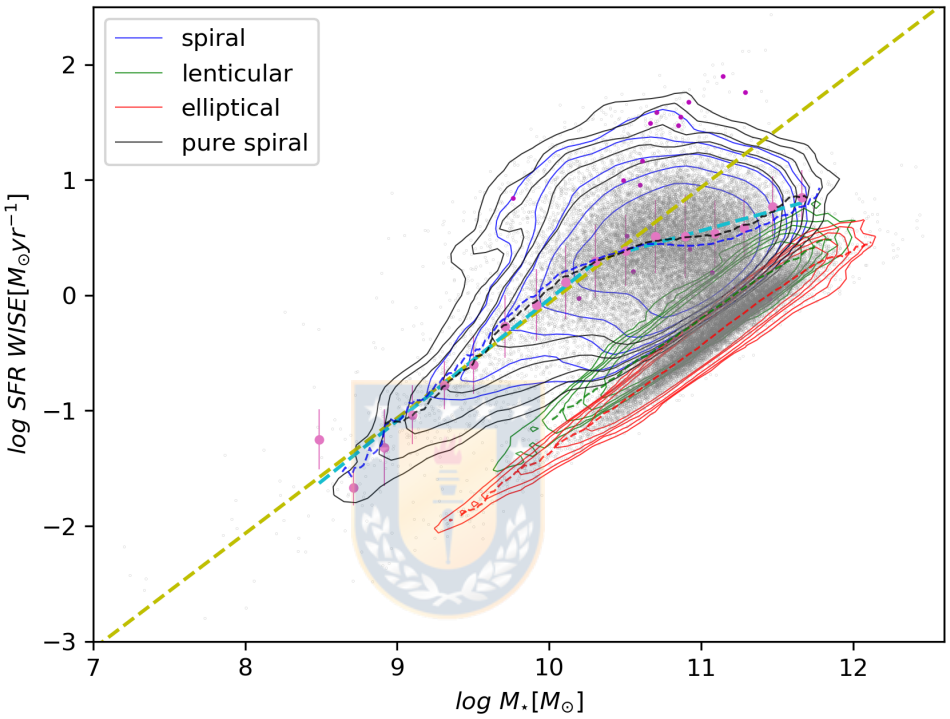

Figura 3.4.1: The Main Sequence (SFR-$M_\star$ plane) of nearby (redshift $z \leq 0.03$) galaxies. SFRs are from W3 and stellar masses from W1 and W2. Grey circles show all galaxies in our 2MRS-WISE sample; magenta circles denote those classified as AGNs by Huchra et al. (2012). The different color contours show the distribution of mophological sub-samples of the 2MRS-WISE sample (see Sect. 3.1): pure-spirals (black), spirals (blue), lenticulars (green) and ellipticals (red). For each sub-sample, we show running-medians (dashed-lines) and standard deviations (as error bars) in the same colors. The mean SFR, and its deviation, of the pure-spirals in each stellar mass bin are shown with pink circles and corresponding error bars. Fitting these pink circles with a broken power-law MS (see text) gives us the final MS, shown with the cyan dashed-line. The yellow dashed-line shows the MS derived by Elbaz et al. (2011) based on SDSS galaxies.

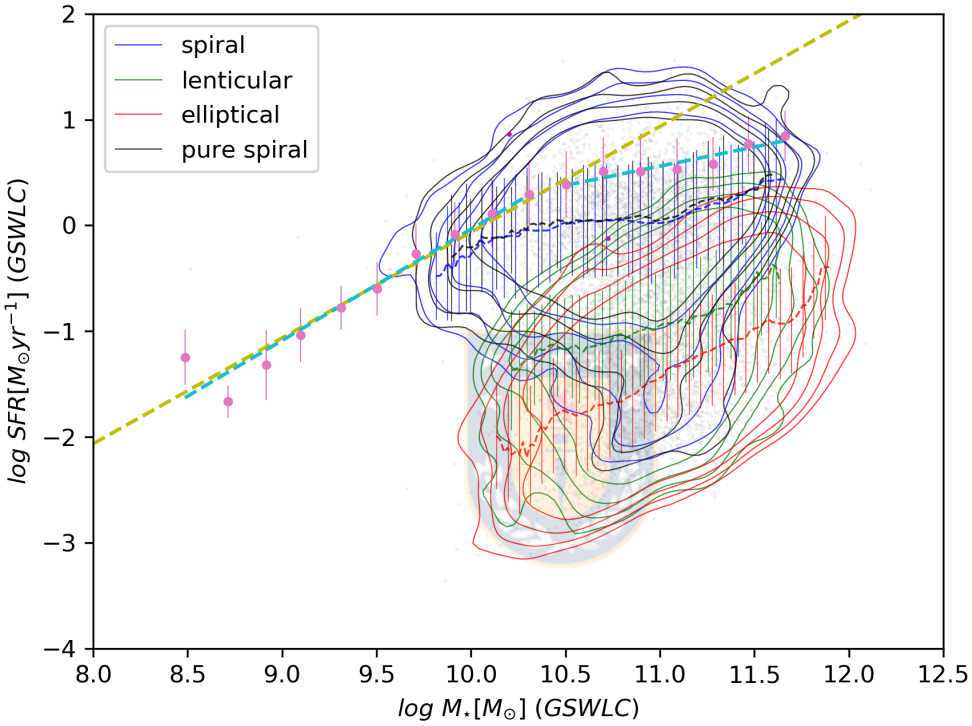

Figura 3.4.2: As in Fig. 3.4.1 but here we only show those galaxies in 2MRS-WISE which also appear in the GSWL Catalog of Salim et al. (2016), and the stellar mass and SFRs of the fit are those from the GSWL Catalog. The pink circles and error bars are the same as in the previous figure. The yellow dashed-line shows the MS as derived by Elbaz et al. (2011), and the pink circles and error bars, plus the cyan dashed-line shows the MS derived by us. Note that the median data for the spiral samples fall below our derived MS. Note also that the GSWL Catalog has very few low stellar mass galaxies as compared to our 2MRS-WISE sample.

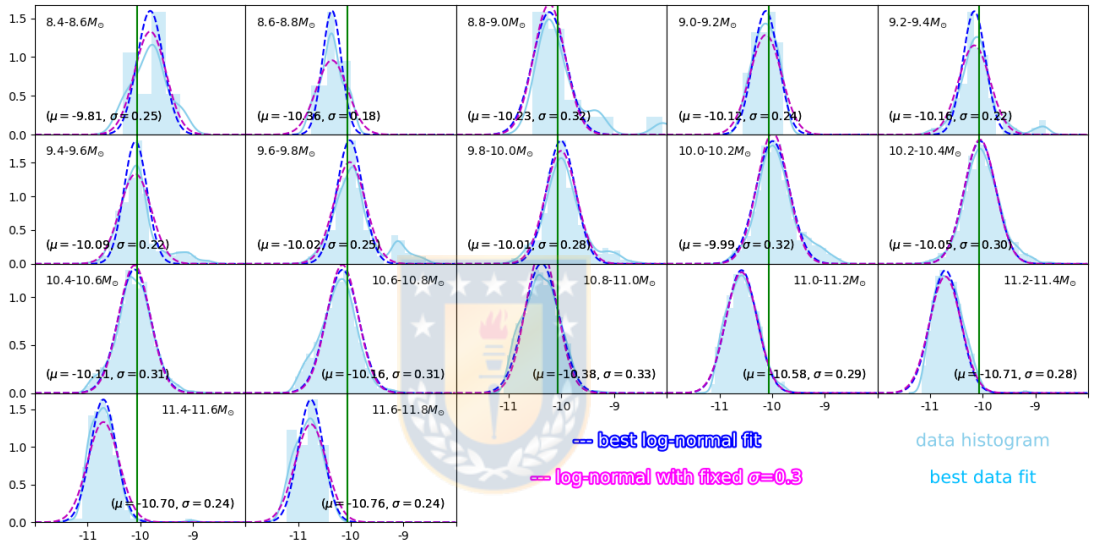

Figura 3.4.3: Normalized histograms of the SSFR of pure-spiral galaxies in the 2MRS-WISE sample, in 18 stellar mass bins from $10^{8.4}$ to $10^{11.8}$M$_\odot$ in steps of 0.2 dex. In each panel, the data is shown in a light blue histogram, and and the best fit to the data is shown in the light blue solid line. The magenta dashed-line shows an expected Gaussian/Normal distribution with a standard deviation of 0.3, while the dark blue dashed-line is the best Gaussian fit using our semi-automated procedure. The constant - over stellar mass - SSFR $\sim 10^{-10}$yr^{-1} predicted by Elbaz et al. (2011) is shown with a vertical green line in each bin.

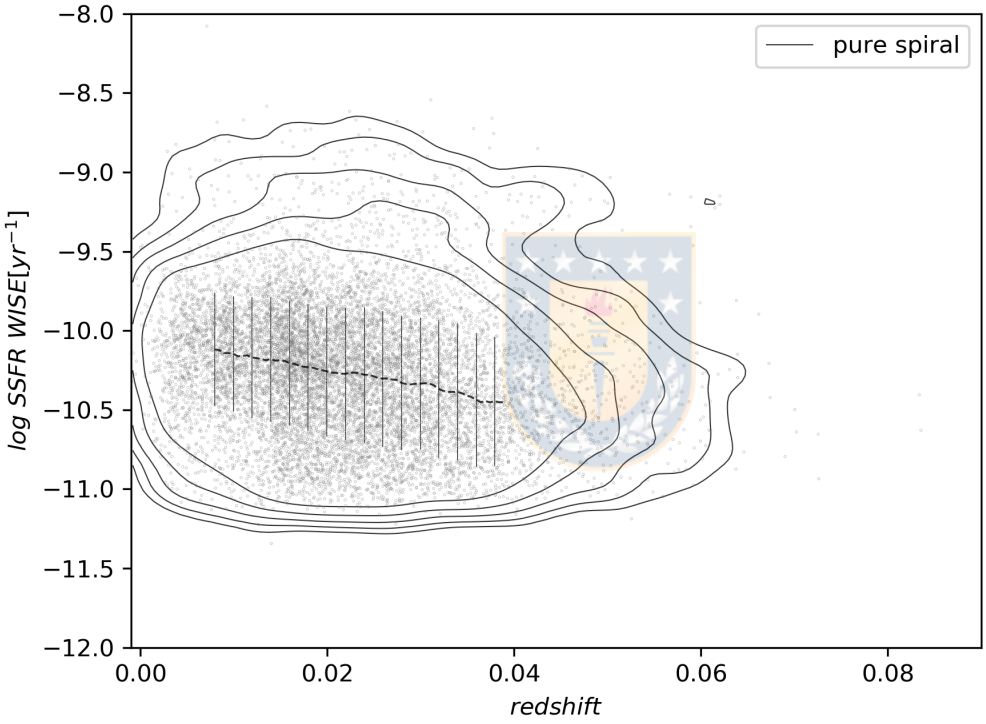

Figura 3.5.1: Specific Star Formation Rate (SSFR) as a function of redshift, for the pure-spiral sample of galaxies (grey circles). Contours (thick lines), running-medians (dashed-lines) and standard deviations (vertical bars) are shown in black colors. The normalization of the peak correspond to the total of pure-spirals.

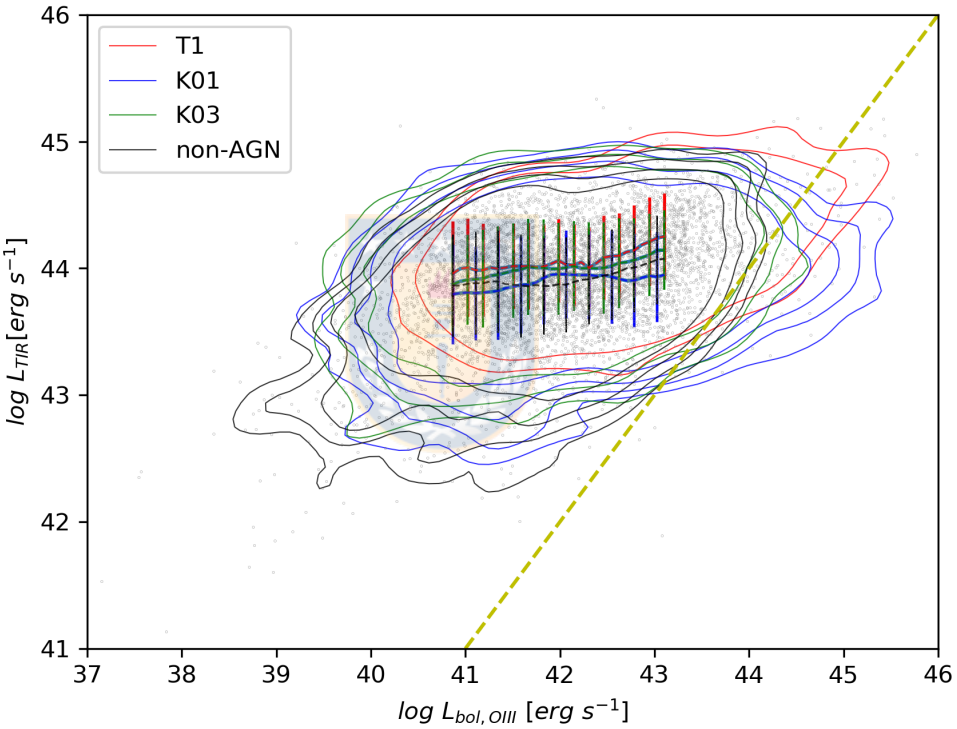

Figura 3.6.1: Comparison between AGN bolometric luminosities $L_{bol,OIII}$ and total IR luminosities L_{TIR}, for the pure-spiral sample, classified by AGN type. The description of contours and data points is the same as in Fig. 3.6.2.

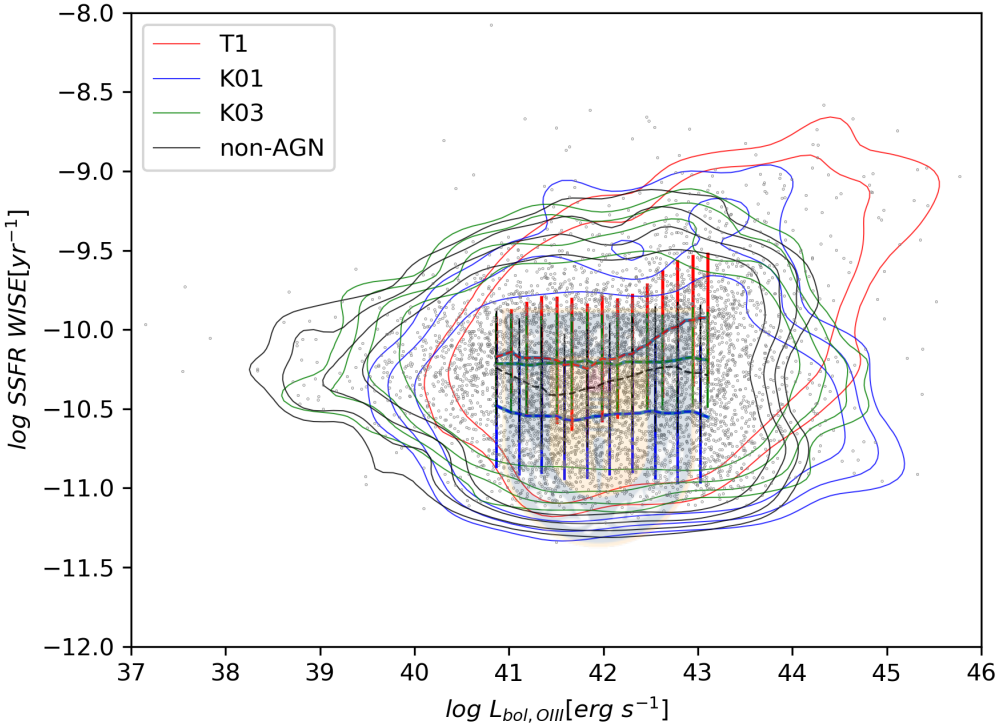

Figura 3.6.2: Specific Star Formation Rate (SSFR) as a function of AGN bolometric luminosities $L_{bol,OIII}$. We show contours for 3 samples of galaxies depending on AGN content: red contours are broad-line AGNs (type 1, denoted as T1), blue contours are narrow-line AGNs (type 2 by Kewley et al., 2001, K01), whilst green contours are narrow-line AGNs (type 2 by Kauffmann et al., 2003, K03). Grey circles correspond to our 2MRS-WISE AGN sample. The diagram show that Seyfert galaxies reach the most extreme values of SSFRs and bolometric luminosities, which is shown by their contours.

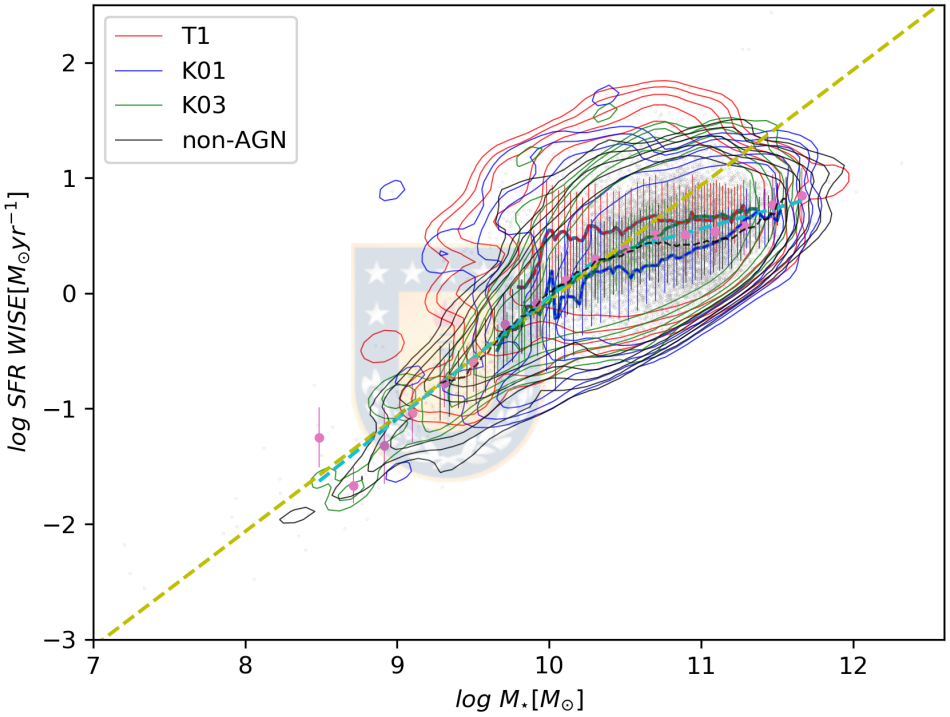

Figura 3.6.3: WISE SFP for the pure-spiral sample classified by AGN type. The yellow dashed-line is the MS of Elbaz et al. (2011) with slope ∼1, while cyan dashed-lines, pink dots and pink bars correspond to our previously derived MS in section 3.4. The description of contours and data points is the same as in Fig. 3.6.2.

Capítulo 4

Discussion and conclusions

In this chapter and hereafter, we obviate the unit system used to describe slopes and normalization (both varying with stellar mass) of the MS, which has been converted to a logarithmic scale. Thus, we summarize our conclusions from previous chapters in the following ideas:

- We determined a low mass MS with slope ∼1.05, which is in good agreement with single power-law best-fits from Elbaz et al. (2011), Wuyts et al. (2011), Brinchmann et al. (2004), Santini et al. (2014) and Gavazzi et al. (2015) who find a low mass slope roughly 1 at low redshift (z∼0). This is also in agreement with Thorne et al. (2020) asymptotic best-fit. At high-z our low mass slope is roughly consistent with Peng et al. (2010), Wuyts et al. (2011), Guo et al. (2013) and Whitaker et al. (2015) single power-law of slope ∼1, also with Whitaker et al. (2014), Schreiber et al. (2015), Lee et al. (2015), Tomczak et al. (2016) and Thorne et al. (2020) who performed broken power-law and asymptotic best-fits with slope roughly 1. We also determined a high mass slope ∼0.36, which is in good agreement with the ones derived by Popesso et al. (2019a) at z∼0. Conversely, when compared to Thorne et al. (2020) results, we assessed an offset of ∼0.11 dex. At high-z, our high mass slope is roughly in agreement with Whitaker et al. (2014), Lee et al. (2015), Gavazzi et al. (2015), Pearson et al. (2018) and Kashino et al. (2019) high mass slopes (up to and offset of ∼0.09) from broken power-law an asymptotic best-fits.
- We found an intercept ~ -10.56 at the low mass end of our MS which is

roughly in agreement with high-z intercept from Guo et al. (2013), who derived a single power-law MS. For low redshift, we determined an intercept ~ -3.43 at the high mass end of the MS, which is in good agreement with those from Popesso et al. (2019a). However, we must add an offset to every W3 SFR calculated in this work, which is denoted as $C_{\rm off}$; it assumes values between 0 to ~ -0.2 dex, indicative of the $\sim$0.2 dex uncertainty from comparing W3 SF to other independent SF tracers.

- We determined turnover of the MS within the range of $10^{10.4}$-$10^{10.6}$M$_\odot$, which is in good agreement with findings of Whitaker et al. (2015), Schreiber et al. (2015) and Popesso et al. (2019a), who determines a turnover mass of $10^{10.5}$M$_\odot$,

- Our derived MS has an intrinsic scatter spanning between $\sim$0.15-0.36 dex., which is in good agreement with low redshift results of Popesso et al. (2019a), although their scatter evolves monotonically from 0.3 dex at 10^{10}M$_\odot$ to 0.45 dex at 10^{11}M$_\odot$. At high-z, we assess consistency with the range of intrinsic scatter determined by Guo et al. (2013), Whitaker et al. (2015), Pearson et al. (2018) and Kashino et al. (2019).

- We found that total IR luminosities from either AGN or normal galaxies in our AGN sample are commonly more powerful than their bolometric luminosities, except for a few exceeding their L$_{\rm TIR}$ by $\sim$1-2 orders of magnitude, which correspond to type 1 and type 2 AGN. These AGN bolometric luminosities resemble those proper of QSOs, showing peaks of bolometric luminosities in the range of $\sim 10^{44}$-10^{46} erg s^{-1}. Additionally, we determined that the AGN type 1 and type 2 (K01) reach the highest SSFRs, with type 1 AGN having a clear peak at $\sim 10^{8.7}$ yr^{-1}. Such high SSFRs coincide with the levels of SF of SB galaxies. From our AGN MS, we see that these high SSFR galaxies are mainly type 1 AGN, with most of AGNs having normal levels of SF. Therefore, we conclude AGN luminosities do not contaminate our SFR sample, except for a few powerful AGN (mostly type 1) that are biasing our MS results, however, we must account for the lack of completeness in this AGN sample.

Bibliografía

(1988). *Infrared Astronomical Satellite (IRAS) Catalogs and Atlases.Volume 1: Explanatory Supplement.*, volume 1.

Alatalo, K., Cales, S. L., Appleton, P. N., Kewley, L. J., Lacy, M., Lisenfeld, U., Nyland, K., and Rich, J. A. (2014). Catching Quenching Galaxies: The Nature of the WISE Infrared Transition Zone. , 794(1):L13.

Antonucci, R. (1993). Unified models for active galactic nuclei and quasars. , 31:473–521.

Assef, R. J., Stern, D., Kochanek, C. S., Blain, A. W., Brodwin, M., Brown, M. J. I., Donoso, E., Eisenhardt, P. R. M., Jannuzi, B. T., Jarrett, T. H., Stanford, S. A., Tsai, C. W., Wu, J., and Yan, L. (2013). Mid-infrared Selection of Active Galactic Nuclei with the Wide-field Infrared Survey Explorer. II. Properties of WISE-selected Active Galactic Nuclei in the NDWFS Boötes Field. , 772(1):26.

Audibert, A., Riffel, R., Sales, D. A., Pastoriza, M. G., and Ruschel-Dutra, D. (2017). Probing the active galactic nucleus unified model torus properties in Seyfert galaxies. , 464(2):2139–2173.

Bianchi, L., Madore, B., Thilker, D., Gil de Paz, A., and GALEX Science Team (2003). The GALEX Nearby Galaxies Survey. In *American Astronomical Society Meeting Abstracts*, volume 203 of *American Astronomical Society Meeting Abstracts*, page 91.12.

Blanton, M. R., Kazin, E., Muna, D., Weaver, B. A., and Price-Whelan, A. (2011). Improved Background Subtraction for the Sloan Digital Sky Survey Images. , 142(1):31.

Boquien, M., Calzetti, D., Kennicutt, R., Dale, D., Engelbracht, C., Gordon, K. D., Hong, S., Lee, J. C., and Portouw, J. (2009). Star-Forming or Starbursting? The Ultraviolet Conundrum. , 706(1):553–570.

Brightman, M., Baloković, M., Ballantyne, D. R., Bauer, F. E., Boorman, P., Buchner, J., Brandt, W. N., Comastri, A., Del Moro, A., Farrah, D., Gandhi, P., Harrison, F. A., Koss, M., Lanz, L., Masini, A., Ricci, C., Stern, D., Vasudevan, R., and Walton, D. J. (2017). X-Ray Bolometric Corrections for Compton-thick Active Galactic Nuclei. , 844(1):10.

Brinchmann, J., Charlot, S., White, S. D. M., Tremonti, C., Kauffmann, G., Heckman, T., and Brinkmann, J. (2004). The physical properties of star-forming galaxies in the low-redshift Universe. , 351(4):1151–1179.

Bruzual A., G. and Charlot, S. (1993). Spectral Evolution of Stellar Populations Using Isochrone Synthesis. , 405:538.

Buat, V., Iglesias-Páramo, J., Seibert, M., Burgarella, D., Charlot, S., Martin, D. C., Xu, C. K., Heckman, T. M., Boissier, S., Boselli, A., Barlow, T., Bianchi, L., Byun, Y. I., Donas, J., Forster, K., Friedman, P. G., Jelinski, P., Lee, Y. W., Madore, B. F., Malina, R., Milliard, B., Morissey, P., Neff, S., Rich, M., Schiminovitch, D., Siegmund, O., Small, T., Szalay, A. S., Welsh, B., and Wyder, T. K. (2005). Dust Attenuation in the Nearby Universe: A Comparison between Galaxies Selected in the Ultraviolet and in the Far-Infrared. , 619(1):L51–L54.

Calderón-Castillo, P., Nagar, N. M., Yi, S., Orellana, G., Chang, Y.-Y., Leiton, R., and Hughes, T. M. (2019). Merging galaxies in isolated environments I. Multiband photometry, classification, stellar masses, and star formation rates. *arXiv e-prints*, page arXiv:1904.09300.

Calzetti, D. (2013). *Star Formation Rate Indicators*, page 419.

Chang, Y.-Y., van der Wel, A., da Cunha, E., and Rix, H.-W. (2015). Stellar Masses and Star Formation Rates for 1M Galaxies from SDSS+WISE. , 219(1):8.

Charlot, S. and Bruzual A, G. (1991). Stellar Population Synthesis Revisited. , 367:126.

Charlot, S., Worthey, G., and Bressan, A. (1996). Uncertainties in the Modeling of Old Stellar Populations. , 457:625.

Cluver, M. E., Jarrett, T. H., Dale, D. A., Smith, J. D. T., August, T., and Brown, M. J. I. (2017). Calibrating Star Formation in WISE Using Total Infrared Luminosity. , 850(1):68.

Cluver, M. E., Jarrett, T. H., Hopkins, A. M., Driver, S. P., Liske, J., Gunawardhana, M. L. P., Taylor, E. N., Robotham, A. S. G., Alpaslan, M., Baldry, I., Brown, M. J. I., Peacock, J. A., Popescu, C. C., Tuffs, R. J., Bauer, A. E., Bland -Hawthorn, J., Colless, M., Holwerda, B. W., Lara-López, M. A., Leschinski, K., López-Sánchez, A. R., Norberg, P., Owers, M. S., Wang, L., and Wilkins, S. M. (2014). Galaxy and Mass Assembly (GAMA): Mid-infrared Properties and Empirical Relations from WISE. , 782(2):90.

Conroy, C., Gunn, J. E., and White, M. (2009). The Propagation of Uncertainties in Stellar Population Synthesis Modeling. I. The Relevance of Uncertain Aspects of Stellar Evolution and the Initial Mass Function to the Derived Physical Properties of Galaxies. , 699(1):486–506.

da Cunha, E., Charlot, S., Dunne, L., Smith, D., and Rowlands, K. (2012). MAGPHYS: a publicly available tool to interpret observed galaxy SEDs. In

Tuffs, R. J. and Popescu, C. C., editors, *The Spectral Energy Distribution of Galaxies - SED 2011*, volume 284, pages 292–296.

da Cunha, E., Charlot, S., and Elbaz, D. (2008). A simple model to interpret the ultraviolet, optical and infrared emission from galaxies. , 388(4):1595–1617.

da Cunha, E., Walter, F., Smail, I. R., Swinbank, A. M., Simpson, J. M., Decarli, R., Hodge, J. A., Weiss, A., van der Werf, P. P., Bertoldi, F., Chapman, S. C., Cox, P., Danielson, A. L. R., Dannerbauer, H., Greve, T. R., Ivison, R. J., Karim, A., and Thomson, A. (2015). An ALMA Survey of Sub-millimeter Galaxies in the Extended Chandra Deep Field South: Physical Properties Derived from Ultraviolet-to-radio Modeling. , 806(1):110.

Daddi, E., Dickinson, M., Morrison, G., Chary, R., Cimatti, A., Elbaz, D., Frayer, D., Renzini, A., Pope, A., Alexander, D. M., Bauer, F. E., Giavalisco, M., Huynh, M., Kurk, J., and Mignoli, M. (2007). Multiwavelength Study of Massive Galaxies at z~2. I. Star Formation and Galaxy Growth. , 670(1):156–172.

Davies, L. J. M., Driver, S. P., Robotham, A. S. G., Grootes, M. W., Popescu, C. C., Tuffs, R. J., Hopkins, A., Alpaslan, M., Andrews, S. K., Bland-Hawthorn, J., Bremer, M. N., Brough, S., Brown, M. J. I., Cluver, M. E., Croom, S., da Cunha, E., Dunne, L., Lara-López, M. A., Liske, J., Loveday, J., Moffett, A. J., Owers, M., Phillipps, S., Sansom, A. E., Taylor, E. N., Michalowski, M. J., Ibar, E., Smith, M., and Bourne, N. (2016). GAMA/H-ATLAS: a meta-analysis of SFR indicators - comprehensive measures of the SFR-M_* relation and cosmic star formation history at z <0.4. , 461(1):458–485.

Davies, L. J. M., Lagos, C. d. P., Katsianis, A., Robotham, A. S. G., Cortese, L., Driver, S. P., Bremer, M. N., Brown, M. J. I., Brough, S., Cluver, M. E., Grootes, M. W., Holwerda, B. W., Owers, M., and Phillipps, S. (2019). Galaxy And Mass Assembly (GAMA): The sSFR-M_* relation part I - σ_{sSFR}-M_* as a function of sample, SFR indicator, and environment. , 483(2):1881–1900.

de Vaucouleurs, G. (1963). Revised Classification of 1500 Bright Galaxies. , 8:31.

Dumas, G., Mundell, C. G., Emsellem, E., and Nagar, N. M. (2007). Central kiloparsec of Seyfert and inactive host galaxies: a comparison of two-dimensional stellar and gaseous kinematics. , 379(4):1249–1278.

Elbaz, D., Daddi, E., Le Borgne, D., Dickinson, M., Alexander, D. M., Chary, R. R., Starck, J. L., Brand t, W. N., Kitzbichler, M., MacDonald, E., Nonino, M., Popesso, P., Stern, D., and Vanzella, E. (2007). The reversal of the star formation-density relation in the distant universe. , 468(1):33–48.

Elbaz, D., Dickinson, M., Hwang, H. S., Díaz-Santos, T., Magdis, G., Magnelli, B., Le Borgne, D., Galliano, F., Pannella, M., Chanial, P., Armus, L., Charmandaris, V., Daddi, E., Aussel, H., Popesso, P., Kartaltepe, J., Altieri, B., Valtchanov, I., Coia, D., Dannerbauer, H., Dasyra, K., Leiton, R., Mazzarella, J., Alexander, D. M., Buat, V., Burgarella, D., Chary, R. R., Gilli, R., Ivison, R. J., Juneau, S., Le Floc'h, E., Lutz, D., Morrison, G. E., Mullaney, J. R., Murphy, E., Pope,

A., Scott, D., Brodwin, M., Calzetti, D., Cesarsky, C., Charlot, S., Dole, H., Eisenhardt, P., Ferguson, H. C., Förster Schreiber, N., Frayer, D., Giavalisco, M., Huynh, M., Koekemoer, A. M., Papovich, C., Reddy, N., Surace, C., Teplitz, H., Yun, M. S., and Wilson, G. (2011). GOODS-Herschel: an infrared main sequence for star-forming galaxies. , 533:A119.

Ezhikode, S. H., Gandhi, P., Done, C., Ward, M., Dewangan, G. C., Misra, R., and Philip, N. S. (2017). Determining the torus covering factors for a sample of type 1 AGN in the local Universe. , 472(3):3492–3511.

Gavazzi, G., Consolandi, G., Dotti, M., Fanali, R., Fossati, M., Fumagalli, M., Viscardi, E., Savorgnan, G., Boselli, A., Gutiérrez, L., Hernández Toledo, H., Giovanelli, R., and Haynes, M. P. (2015). Hα3: an Hα imaging survey of HI selected galaxies from ALFALFA. VI. The role of bars in quenching star formation from z = 3 to the present epoch. , 580:A116.

Gehrz, R. (1989). Sources of Stardust in the Galaxy. In Allamandola, L. J. and Tielens, A. G. G. M., editors, *Interstellar Dust*, volume 135, page 445.

Genel, S., Vogelsberger, M., Springel, V., Sijacki, D., Nelson, D., Snyder, G., Rodriguez-Gomez, V., Torrey, P., and Hernquist, L. (2014). Introducing the Illustris project: the evolution of galaxy populations across cosmic time. , 445(1):175–200.

Genzel, R., Tacconi, L. J., Gracia-Carpio, J., Sternberg, A., Cooper, M. C., Shapiro, K., Bolatto, A., Bouché, N., Bournaud, F., Burkert, A., Combes, F., Comerford, J., Cox, P., Davis, M., Förster Schreiber, N. M., Garcia-Burillo, S., Lutz, D., Naab, T., Neri, R., Omont, A., Shapley, A., and Weiner, B. (2010). A study of the gas-star formation relation over cosmic time. , 407(4):2091–2108.

Gil de Paz, A., Boissier, S., Madore, B. F., Seibert, M., Joe, Y. H., Boselli, A., Wyder, T. K., Thilker, D., Bianchi, L., Rey, S.-C., Rich, R. M., Barlow, T. A., Conrow, T., Forster, K., Friedman, P. G., Martin, D. C., Morrissey, P., Neff, S. G., Schiminovich, D., Small, T., Donas, J., Heckman, T. M., Lee, Y.-W., Milliard, B., Szalay, A. S., and Yi, S. (2007). The GALEX Ultraviolet Atlas of Nearby Galaxies. , 173(2):185–255.

Gil de Paz, A., Madore, B. F., Boissier, S., and GALEX Science Team (2004). First Results from the GALEX Nearby Galaxies Survey. In *American Astronomical Society Meeting Abstracts*, volume 205 of *American Astronomical Society Meeting Abstracts*, page 42.01.

Guo, K., Zheng, X. Z., and Fu, H. (2013). The Intrinsic Scatter along the Main Sequence of Star-forming Galaxies at z ~0.7. , 778(1):23.

Hayward, C. C. and Smith, D. J. B. (2015). Should we believe the results of ultraviolet-millimetre galaxy spectral energy distribution modelling? , 446(2):1512–1535.

Heckman, T. M., Kauffmann, G., Brinchmann, J., Charlot, S., Tremonti, C., and White, S. D. M. (2004). Present-Day Growth of Black Holes and Bulges: The Sloan Digital Sky Survey Perspective. , 613(1):109–118.

Henriques, B. M. B., White, S. D. M., Thomas, P. A., Angulo, R., Guo, Q., Lemson, G., Springel, V., and Overzier, R. (2015). Galaxy formation in the Planck cosmology - I. Matching the observed evolution of star formation rates, colours and stellar masses. , 451(3):2663–2680.

Huchra, J., Jarrett, T., Skrutskie, M., Cutri, R., Schneider, S., Macri, L., Steining, R., Mader, J., Martimbeau, N., and George, T. (2005). The 2MASS Redshift Survey and Low Galactic Latitude Large-Scale Structure. In Fairall, A. P. and Woudt, P. A., editors, *Nearby Large-Scale Structures and the Zone of Avoidance*, volume 329 of *Astronomical Society of the Pacific Conference Series*, page 135.

Huchra, J. P., Macri, L. M., Masters, K. L., Jarrett, T. H., Berlind, P., Calkins, M., Crook, A. C., Cutri, R., Erdoğdu, P., Falco, E., George, T., Hutcheson, C. M., Lahav, O., Mader, J., Mink, J. D., Martimbeau, N., Schneider, S., Skrutskie, M., Tokarz, S., and Westover, M. (2012). The 2MASS Redshift Survey—Description and Data Release. , 199(2):26.

Jarrett, T. (2004). Large Scale Structure in the Local Universe - The 2MASS Galaxy Catalog. , 21(4):396–403.

Jarrett, T. H., Chester, T., Cutri, R., Schneider, S., Skrutskie, M., and Huchra, J. P. (2000). 2MASS Extended Source Catalog: Overview and Algorithms. , 119(5):2498–2531.

Jarrett, T. H., Cluver, M. E., Magoulas, C., Bilicki, M., Alpaslan, M., Bland-Hawthorn, J., Brough, S., Brown, M. J. I., Croom, S., Driver, S., Holwerda, B. W., Hopkins, A. M., Loveday, J., Norberg, P., Peacock, J. A., Popescu, C. C., Sadler, E. M., Taylor, E. N., Tuffs, R. J., and Wang, L. (2017). Galaxy and Mass Assembly (GAMA): Exploring the WISE Web in G12. , 836(2):182.

Jarrett, T. H., Cohen, M., Masci, F., Wright, E., Stern, D., Benford, D., Blain, A., Carey, S., Cutri, R. M., Eisenhardt, P., Lonsdale, C., Mainzer, A., Marsh, K., Padgett, D., Petty, S., Ressler, M., Skrutskie, M., Stanford, S., Surace, J., Tsai, C. W., Wheelock, S., and Yan, D. L. (2011). The Spitzer-WISE Survey of the Ecliptic Poles. , 735(2):112.

Jarrett, T. H., Masci, F., Tsai, C. W., Petty, S., Cluver, M. E., Assef, R. J., Benford, D., Blain, A., Bridge, C., Donoso, E., Eisenhardt, P., Koribalski, B., Lake, S., Neill, J. D., Seibert, M., Sheth, K., Stanford, S., and Wright, E. (2013). Extending the Nearby Galaxy Heritage with WISE: First Results from the WISE Enhanced Resolution Galaxy Atlas. , 145(1):6.

Karim, A., Schinnerer, E., Martínez-Sansigre, A., Sargent, M. T., van der Wel, A., Rix, H. W., Ilbert, O., Smolčić, V., Carilli, C., Pannella, M., Koekemoer, A. M., Bell, E. F., and Salvato, M. (2011). The Star Formation History of Mass-selected Galaxies in the COSMOS Field. , 730(2):61.

Kashino, D., Silverman, J. D., Rodighiero, G., Renzini, A., Arimoto, N., Daddi, E., Lilly, S. J., Sanders, D. B., Kartaltepe, J., Zahid, H. J., Nagao, T., Sugiyama, N., Capak, P., Carollo, C. M., Chu, J., Hasinger, G., Ilbert, O., Kajisawa, M., Kewley, L. J., Koekemoer, A. M., Kovač, K., Le Fèvre, O., Masters, D., McCracken, H. J., Onodera, M., Scoville, N., Strazzullo, V., Symeonidis, M., and Taniguchi, Y. (2013). The FMOS-COSMOS Survey of Star-forming Galaxies at z ~1.6. I. Hα-based Star Formation Rates and Dust Extinction. , 777(1):L8.

Kashino, D., Silverman, J. D., Sanders, D., Kartaltepe, J., Daddi, E., Renzini, A., Rodighiero, G., Puglisi, A., Valentino, F., Juneau, S., Arimoto, N., Nagao, T., Ilbert, O., Le Fèvre, O., and Koekemoer, A. M. (2019). The FMOS-COSMOS Survey of Star-forming Galaxies at z $\sim$ 1.6. VI. Redshift and Emission-line Catalog and Basic Properties of Star-forming Galaxies. , 241(1):10.

Kauffmann, G., Heckman, T. M., Tremonti, C., Brinchmann, J., Charlot, S., White, S. D. M., Ridgway, S. E., Brinkmann, J., Fukugita, M., Hall, P. B., Ivezić, Ž., Richards, G. T., and Schneider, D. P. (2003). The host galaxies of active galactic nuclei. , 346(4):1055–1077.

Kennicutt, Robert C., J. (1988). Properties of H II Region Populations in Galaxies. I. The First-ranked H II Regions. , 334:144.

Kennicutt, Robert C., J. (1998). The Global Schmidt Law in Star-forming Galaxies. , 498(2):541–552.

Kennicutt, Robert C., J., Hao, C.-N., Calzetti, D., Moustakas, J., Dale, D. A., Bendo, G., Engelbracht, C. W., Johnson, B. D., and Lee, J. C. (2009). Dust-corrected Star Formation Rates of Galaxies. I. Combinations of Hα and Infrared Tracers. , 703(2):1672–1695.

Kennicutt, R. C. and Evans, N. J. (2012). Star Formation in the Milky Way and Nearby Galaxies. , 50:531–608.

Kewley, L. J., Dopita, M. A., Sutherland, R. S., Heisler, C. A., and Trevena, J. (2001). Theoretical Modeling of Starburst Galaxies. , 556(1):121–140.

Kong, X., Charlot, S., Brinchmann, J., and Fall, S. M. (2004). Star formation history and dust content of galaxies drawn from ultraviolet surveys. , 349(3):769–778.

Kormendy, J. and Bender, R. (2012). A Revised Parallel-sequence Morphological Classification of Galaxies: Structure and Formation of S0 and Spheroidal Galaxies. , 198(1):2.

Kourkchi, E., Courtois, H. M., Graziani, R., Hoffman, Y., Pomarède, D., Shaya, E. J., and Tully, R. B. (2020). Cosmicflows-3: Two Distance-Velocity Calculators. , 159(2):67.

Kroupa, P. (2001). On the variation of the initial mass function. , 322(2):231–246.

Kurczynski, P., Gawiser, E., Acquaviva, V., Bell, E. F., Dekel, A., de Mello, D. F., Ferguson, H. C., Gardner, J. P., Grogin, N. A., Guo, Y., Hopkins, P. F., Koekemoer, A. M., Koo, D. C., Lee, S.-K., Mobasher, B., Primack, J. R., Rafelski, M., Soto, E., and Teplitz, H. I. (2016). Evolution of Intrinsic Scatter in the SFR-Stellar Mass Correlation at 0.5 <z <3. , 820(1):L1.

Lake, S. E., Wright, E. L., Petty, S., Assef, R. J., Jarrett, T. H., Stanford, S. A., Stern, D., and Tsai, C. W. (2012). Optical Spectroscopic Survey of High-latitude WISE-selected Sources. , 143(1):7.

Lee, N., Sanders, D. B., Casey, C. M., Toft, S., Scoville, N. Z., Hung, C.-L., Le Floc'h, E., Ilbert, O., Zahid, H. J., Aussel, H., Capak, P., Kartaltepe, J. S., Kewley, L. J., Li, Y., Schawinski, K., Sheth, K., and Xiao, Q. (2015). A Turnover in the Galaxy Main Sequence of Star Formation at M $_*$ ~10^{10} M for Redshifts z <1.3. , 801(2):80.

Mancini, C., Renzini, A., Daddi, E., Rodighiero, G., Berta, S., Grogin, N., Kocevski, D., and Koekemoer, A. (2015). Star formation and quenching among the most massive galaxies at z $\sim$ 1.7. , 450(1):763–786.

Marleau, F. R., Clancy, D., Habas, R., and Bianconi, M. (2017). Infrared signature of active massive black holes in nearby dwarf galaxies. , 602:A28.

Mateos, S., Alonso-Herrero, A., Carrera, F. J., Blain, A., Watson, M. G., Barcons, X., Braito, V., Severgnini, P., Donley, J. L., and Stern, D. (2012). Using the Bright Ultrahard XMM-Newton survey to define an IR selection of luminous AGN based on WISE colours. , 426(4):3271–3281.

Meurer, G. R., Heckman, T. M., and Calzetti, D. (1999). Dust Absorption and the Ultraviolet Luminosity Density at z ~3 as Calibrated by Local Starburst Galaxies. , 521(1):64–80.

Mingo, B., Watson, M. G., Rosen, S. R., Hardcastle, M. J., Ruiz, A., Blain, A., Carrera, F. J., Mateos, S., Pineau, F. X., and Stewart, G. C. (2016). The MIXR sample: AGN activity versus star formation across the cross-correlation of WISE, 3XMM, and FIRST/NVSS. , 462(3):2631–2667.

Netzer, H., Lutz, D., Schweitzer, M., Contursi, A., Sturm, E., Tacconi, L. J., Veilleux, S., Kim, D. C., Rupke, D., Baker, A. J., Dasyra, K., Mazzarella, J., and Lord, S. (2007). Spitzer Quasar and ULIRG Evolution Study (QUEST). II. The Spectral Energy Distributions of Palomar-Green Quasars. , 666(2):806–816.

Neugebauer, G., Habing, H. J., van Duinen, R., Aumann, H. H., Baud, B., Beichman, C. A., Beintema, D. A., Boggess, N., Clegg, P. E., de Jong, T., Emerson, J. P., Gautier, T. N., Gillett, F. C., Harris, S., Hauser, M. G., Houck, J. R., Jennings, R. E., Low, F. J., Marsden, P. L., Miley, G., Olnon, F. M., Pottasch, S. R., Raimond, E., Rowan-Robinson, M., Soifer, B. T., Walker, R. G., Wesselius, P. R., and Young, E. (1984). The Infrared Astronomical Satellite (IRAS) mission. , 278:L1–L6.

Noeske, K. G., Weiner, B. J., Faber, S. M., Papovich, C., Koo, D. C., Somerville, R. S., Bundy, K., Conselice, C. J., Newman, J. A., Schiminovich, D., Le Floc'h, E., Coil, A. L., Rieke, G. H., Lotz, J. M., Primack, J. R., Barmby, P., Cooper, M. C., Davis, M., Ellis, R. S., Fazio, G. G., Guhathakurta, P., Huang, J., Kassin, S. A., Martin, D. C., Phillips, A. C., Rich, R. M., Small, T. A., Willmer, C. N. A., and Wilson, G. (2007). Star Formation in AEGIS Field Galaxies since z=1.1: The Dominance of Gradually Declining Star Formation, and the Main Sequence of Star-forming Galaxies. , 660(1):L43–L46.

Ogle, P. M., Lanz, L., Appleton, P. N., Helou, G., and Mazzarella, J. (2019). A Catalog of the Most Optically Luminous Galaxies at z <0.3: Super Spirals, Super Lenticulars, Super Post-mergers, and Giant Ellipticals. , 243(1):14.

Oh, K., Yi, S. K., Schawinski, K., Koss, M., Trakhtenbrot, B., and Soto, K. (2015). A New Catalog of Type 1 AGNs and its Implications on the AGN Unified Model. , 219(1):1.

Orellana, G., Nagar, N. M., Elbaz, D., Calderón-Castillo, P., Leiton, R., Ibar, E., Magnelli, B., Daddi, E., Messias, H., Cerulo, P., and Slater, R. (2017). Molecular gas, dust, and star formation in galaxies. I. Dust properties and scalings in 1600 nearby galaxies. , 602:A68.

Pannella, M., Elbaz, D., Daddi, E., Dickinson, M., Hwang, H. S., Schreiber, C., Strazzullo, V., Aussel, H., Bethermin, M., Buat, V., Charmandaris, V., Cibinel, A., Juneau, S., Ivison, R. J., Le Borgne, D., Le Floc'h, E., Leiton, R., Lin, L., Magdis, G., Morrison, G. E., Mullaney, J., Onodera, M., Renzini, A., Salim, S., Sargent, M. T., Scott, D., Shu, X., and Wang, T. (2015). GOODS-Herschel: Star Formation, Dust Attenuation, and the FIR-radio Correlation on the Main Sequence of Star-forming Galaxies up to z 4. , 807(2):141.

Pearson, W. J., Wang, L., Hurley, P. D., Małek, K., Buat, V., Burgarella, D., Farrah, D., Oliver, S. J., Smith, D. J. B., and van der Tak, F. F. S. (2018). Main sequence of star forming galaxies beyond the Herschel confusion limit. , 615:A146.

Peng, Y.-j., Lilly, S. J., Kovač, K., Bolzonella, M., Pozzetti, L., Renzini, A., Zamorani, G., Ilbert, O., Knobel, C., Iovino, A., Maier, C., Cucciati, O., Tasca, L., Carollo, C. M., Silverman, J., Kampczyk, P., de Ravel, L., Sanders, D., Scoville, N., Contini, T., Mainieri, V., Scodeggio, M., Kneib, J.-P., Le Fèvre, O., Bardelli, S., Bongiorno, A., Caputi, K., Coppa, G., de la Torre, S., Franzetti, P., Garilli, B., Lamareille, F., Le Borgne, J.-F., Le Brun, V., Mignoli, M., Perez Montero, E., Pello, R., Ricciardelli, E., Tanaka, M., Tresse, L., Vergani, D., Welikala, N., Zucca, E., Oesch, P., Abbas, U., Barnes, L., Bordoloi, R., Bottini, D., Cappi, A., Cassata, P., Cimatti, A., Fumana, M., Hasinger, G., Koekemoer, A., Leauthaud, A., Maccagni, D., Marinoni, C., McCracken, H., Memeo, P., Meneux, B., Nair, P., Porciani, C., Presotto, V., and Scaramella, R. (2010). Mass and Environment as Drivers of Galaxy Evolution in SDSS and zCOSMOS and the Origin of the Schechter Function. , 721(1):193–221.

Popesso, P., Concas, A., Morselli, L., Schreiber, C., Rodighiero, G., Cresci, G., Belli, S., Erfanianfar, G., Mancini, C., Inami, H., Dickinson, M., Ilbert, O., Pannella, M., and Elbaz, D. (2019a). The main sequence of star-forming galaxies - I. The local relation and its bending. , 483(3):3213–3226.

Popesso, P., Morselli, L., Concas, A., Schreiber, C., Rodighiero, G., Cresci, G., Belli, S., Ilbert, O., Erfanianfar, G., Mancini, C., Inami, H., Dickinson, M., Pannella, M., and Elbaz, D. (2019b). The main sequence of star-forming galaxies - II. A non-evolving slope at the high-mass end. , 490(4):5285–5299.

Popesso, P., Rodighiero, G., Saintonge, A., Santini, P., Grazian, A., Lutz, D., Brusa, M., Altieri, B., Andreani, P., Aussel, H., Berta, S., Bongiovanni, A., Cava, A., Cepa, J., Cimatti, A., Daddi, E., Dominguez, H., Elbaz, D., Förster Schreiber, N., Genzel, R., Gruppioni, C., Magdis, G., Maiolino, R., Magnelli, B., Nordon, R., Pérez García, A. M., Poglitsch, A., Pozzi, F., Riguccini, L., Sanchez-Portal, M., Shao, L., Sturm, E., Tacconi, L., Valtchanov, I., Wieprecht, E., and Wetzstein, M. (2011). The effect of environment on star forming galaxies at redshift. I. First insight from PACS. , 532:A145.

Puglisi, A., Daddi, E., Liu, D., Bournaud, F., Silverman, J. D., Circosta, C., Calabrò, A., Aravena, M., Cibinel, A., Dannerbauer, H., Delvecchio, I., Elbaz, D., Gao, Y., Gobat, R., Jin, S., Le Floc'h, E., Magdis, G. E., Mancini, C., Riechers, D. A., Rodighiero, G., Sargent, M., Valentino, F., and Zanisi, L. (2019). The Main Sequence at z $\sim$ 1.3 Contains a Sizable Fraction of Galaxies with Compact Star Formation Sizes: A New Population of Early Post-starbursts? , 877(2):L23.

Punsly, B. and Zhang, S. (2011). Calibrating emission lines as quasar bolometers. , 412(1):L123–L127.

Renzini, A. and Peng, Y.-j. (2015). An Objective Definition for the Main Sequence of Star-forming Galaxies. , 801(2):L29.

Rodighiero, G., Cimatti, A., Gruppioni, C., Popesso, P., Andreani, P., Altieri, B., Aussel, H., Berta, S., Bongiovanni, A., Brisbin, D., Cava, A., Cepa, J., Daddi, E., Dominguez-Sanchez, H., Elbaz, D., Fontana, A., Förster Schreiber, N., Franceschini, A., Genzel, R., Grazian, A., Lutz, D., Magdis, G., Magliocchetti, M., Magnelli, B., Maiolino, R., Mancini, C., Nordon, R., Perez Garcia, A. M., Poglitsch, A., Santini, P., Sanchez-Portal, M., Pozzi, F., Riguccini, L., Saintonge, A., Shao, L., Sturm, E., Tacconi, L., Valtchanov, I., Wetzstein, M., and Wieprecht, E. (2010). The first Herschel view of the mass-SFR link in high-z galaxies. , 518:L25.

Rodighiero, G., Daddi, E., Baronchelli, I., Cimatti, A., Renzini, A., Aussel, H., Popesso, P., Lutz, D., Andreani, P., Berta, S., Cava, A., Elbaz, D., Feltre, A., Fontana, A., Förster Schreiber, N. M., Franceschini, A., Genzel, R., Grazian, A., Gruppioni, C., Ilbert, O., Le Floch, E., Magdis, G., Magliocchetti, M., Magnelli, B., Maiolino, R., McCracken, H., Nordon, R., Poglitsch, A., Santini, P., Pozzi,

F., Riguccini, L., Tacconi, L. J., Wuyts, S., and Zamorani, G. (2011). The Lesser Role of Starbursts in Star Formation at z = 2. , 739(2):L40.

Rodighiero, G., Renzini, A., Daddi, E., Baronchelli, I., Berta, S., Cresci, G., Franceschini, A., Gruppioni, C., Lutz, D., Mancini, C., Santini, P., Zamorani, G., Silverman, J., Kashino, D., Andreani, P., Cimatti, A., Sánchez, H. D., Le Floch, E., Magnelli, B., Popesso, P., and Pozzi, F. (2014). A multiwavelength consensus on the main sequence of star-forming galaxies at z ∼ 2. , 443(1):19–30.

Salim, S., Boquien, M., and Lee, J. C. (2018). Dust Attenuation Curves in the Local Universe: Demographics and New Laws for Star-forming Galaxies and High-redshift Analogs. , 859(1):11.

Salim, S., Lee, J. C., Janowiecki, S., da Cunha, E., Dickinson, M., Boquien, M., Burgarella, D., Salzer, J. J., and Charlot, S. (2016). GALEX-SDSS-WISE Legacy Catalog (GSWLC): Star Formation Rates, Stellar Masses, and Dust Attenuations of 700,000 Low-redshift Galaxies. , 227(1):2.

Santini, P., Fontana, A., Grazian, A., Salimbeni, S., Fiore, F., Fontanot, F., Boutsia, K., Castellano, M., Cristiani, S., de Santis, C., Gallozzi, S., Giallongo, E., Menci, N., Nonino, M., Paris, D., Pentericci, L., and Vanzella, E. (2009). Star formation and mass assembly in high redshift galaxies. , 504(3):751–767.

Santini, P., Maiolino, R., Magnelli, B., Lutz, D., Lamastra, A., Li Causi, G., Eales, S., Andreani, P., Berta, S., Buat, V., Cooray, A., Cresci, G., Daddi, E., Farrah, D., Fontana, A., Franceschini, A., Genzel, R., Granato, G., Grazian, A., Le Floc'h, E., Magdis, G., Magliocchetti, M., Mannucci, F., Menci, N., Nordon, R., Oliver, S., Popesso, P., Pozzi, F., Riguccini, L., Rodighiero, G., Rosario, D. J., Salvato, M., Scott, D., Silva, L., Tacconi, L., Viero, M., Wang, L., Wuyts, S., and Xu, K. (2014). The evolution of the dust and gas content in galaxies. , 562:A30.

Schawinski, K., Urry, C. M., Simmons, B. D., Fortson, L., Kaviraj, S., Keel, W. C., Lintott, C. J., Masters, K. L., Nichol, R. C., Sarzi, M., Skibba, R., Treister, E., Willett, K. W., Wong, O. I., and Yi, S. K. (2014). The green valley is a red herring: Galaxy Zoo reveals two evolutionary pathways towards quenching of star formation in early- and late-type galaxies. , 440(1):889–907.

Schreiber, C., Pannella, M., Elbaz, D., Béthermin, M., Inami, H., Dickinson, M., Magnelli, B., Wang, T., Aussel, H., Daddi, E., Juneau, S., Shu, X., Sargent, M. T., Buat, V., Faber, S. M., Ferguson, H. C., Giavalisco, M., Koekemoer, A. M., Magdis, G., Morrison, G. E., Papovich, C., Santini, P., and Scott, D. (2015). The Herschel view of the dominant mode of galaxy growth from z = 4 to the present day. , 575:A74.

Scott, A. E. and Stewart, G. C. (2014). Do the spectral energy distributions of type 1 active galactic nuclei show diversity? , 438(3):2253–2266.

Skrutskie, M. F., Cutri, R. M., Stiening, R., Weinberg, M. D., Schneider, S., Carpenter, J. M., Beichman, C., Capps, R., Chester, T., Elias, J., Huchra,

J., Liebert, J., Lonsdale, C., Monet, D. G., Price, S., Seitzer, P., Jarrett, T., Kirkpatrick, J. D., Gizis, J. E., Howard, E., Evans, T., Fowler, J., Fullmer, L., Hurt, R., Light, R., Kopan, E. L., Marsh, K. A., McCallon, H. L., Tam, R., Van Dyk, S., and Wheelock, S. (2006). The Two Micron All Sky Survey (2MASS). , 131(2):1163–1183.

Speagle, J. S., Steinhardt, C. L., Capak, P. L., and Silverman, J. D. (2014). A Highly Consistent Framework for the Evolution of the Star-Forming "Main Sequence" from z ~0-6. , 214(2):15.

Steinhardt, C. L., Speagle, J. S., Capak, P., Silverman, J. D., Carollo, M., Dunlop, J., Hashimoto, Y., Hsieh, B.-C., Ilbert, O., Le Fevre, O., Le Floc'h, E., Lee, N., Lin, L., Lin, Y.-T., Masters, D., McCracken, H. J., Nagao, T., Petric, A., Salvato, M., Sanders, D., Scoville, N., Sheth, K., Strauss, M. A., and Taniguchi, Y. (2014). Star Formation at 4 <z <6 from the Spitzer Large Area Survey with Hyper-Suprime-Cam (SPLASH). , 791(2):L25.

Stern, D., Assef, R. J., Benford, D. J., Blain, A., Cutri, R., Dey, A., Eisenhardt, P., Griffith, R. L., Jarrett, T. H., Lake, S., Masci, F., Petty, S., Stanford, S. A., Tsai, C.-W., Wright, E. L., Yan, L., Harrison, F., and Madsen, K. (2012). Mid-infrared Selection of Active Galactic Nuclei with the Wide-Field Infrared Survey Explorer. I. Characterizing WISE-selected Active Galactic Nuclei in COSMOS. , 753(1):30.

Strauss, M. A., Weinberg, D. H., Lupton, R. H., Narayanan, V. K., Annis, J., Bernardi, M., Blanton, M., Burles, S., Connolly, A. J., Dalcanton, J., Doi, M., Eisenstein, D., Frieman, J. A., Fukugita, M., Gunn, J. E., Ivezić, Ž., Kent, S., Kim, R. S. J., Knapp, G. R., Kron, R. G., Munn, J. A., Newberg, H. J., Nichol, R. C., Okamura, S., Quinn, T. R., Richmond, M. W., Schlegel, D. J., Shimasaku, K., SubbaRao, M., Szalay, A. S., Vanden Berk, D., Vogeley, M. S., Yanny, B., Yasuda, N., York, D. G., and Zehavi, I. (2002). Spectroscopic Target Selection in the Sloan Digital Sky Survey: The Main Galaxy Sample. , 124(3):1810–1824.

Tacchella, S., Carollo, C. M., Renzini, A., Schreiber, N. M. F., Lang, P., Wuyts, S., Cresci, G., Dekel, A., Genzel, R., Lilly, S. J., Mancini, C., Newman, S., Onodera, M., Shapley, A., Tacconi, L., Woo, J., and Zamorani, G. (2015). Evidence for mature bulges and an inside-out quenching phase 3 billion years after the Big Bang. *Science*, 348(6232):314–317.

Thorne, J. E., Robotham, A. S. G., Davies, L. J. M., Bellstedt, S., Driver, S. P., Bravo, M., Bremer, M. N., Holwerda, B. W., Hopkins, A. M., Lagos, C. d. P., Phillipps, S., Siudek, M., Taylor, E. N., and Wright, A. H. (2020). Deep Extragalactic VIsible Legacy Survey (DEVILS): SED Fitting in the D10-COSMOS Field and the Evolution of the Stellar Mass Function and SFR-$M_\star$ relation. *arXiv e-prints*, page arXiv:2011.13605.

Tomczak, A. R., Quadri, R. F., Tran, K.-V. H., Labbé, I., Straatman, C. M. S., Papovich, C., Glazebrook, K., Allen, R., Brammer, G. B., Cowley, M., Dickinson, M., Elbaz, D., Inami, H., Kacprzak, G. G., Morrison, G. E., Nanayakkara, T.,

Persson, S. E., Rees, G. A., Salmon, B., Schreiber, C., Spitler, L. R., and Whitaker, K. E. (2016). The SFR-M* Relation and Empirical Star-Formation Histories from ZFOURGE* at 0.5 <z <4. , 817(2):118.

Toomre, A. and Toomre, J. (1972). Galactic Bridges and Tails. , 178:623–666.

Vogelsberger, M., Genel, S., Springel, V., Torrey, P., Sijacki, D., Xu, D., Snyder, G., Nelson, D., and Hernquist, L. (2014). Introducing the Illustris Project: simulating the coevolution of dark and visible matter in the Universe. , 444(2):1518–1547.

Wang, L., Norberg, P., Gunawardhana, M. L. P., Heinis, S., Baldry, I. K., Bland-Hawthorn, J., Bourne, N., Brough, S., Brown, M. J. I., Cluver, M. E., Cooray, A., da Cunha, E., Driver, S. P., Dunne, L., Dye, S., Eales, S., Grootes, M. W., Holwerda, B. W., Hopkins, A. M., Ibar, E., Ivison, R., Lacey, C., Lara-Lopez, M. A., Loveday, J., Maddox, S. J., Michałowski, M. J., Oteo, I., Owers, M. S., Popescu, C. C., Smith, D. J. B., Taylor, E. N., Tuffs, R. J., and van der Werf, P. (2016). GAMA/H-ATLAS: common star formation rate indicators and their dependence on galaxy physical parameters. , 461(2):1898–1916.

Whitaker, K. E., Franx, M., Bezanson, R., Brammer, G. B., van Dokkum, P. G., Kriek, M. T., Labbé, I., Leja, J., Momcheva, I. G., Nelson, E. J., Rigby, J. R., Rix, H.-W., Skelton, R. E., van der Wel, A., and Wuyts, S. (2015). Galaxy Structure as a Driver of the Star Formation Sequence Slope and Scatter. , 811(1):L12.

Whitaker, K. E., Franx, M., Leja, J., van Dokkum, P. G., Henry, A., Skelton, R. E., Fumagalli, M., Momcheva, I. G., Brammer, G. B., Labbé, I., Nelson, E. J., and Rigby, J. R. (2014). Constraining the Low-mass Slope of the Star Formation Sequence at 0.5 <z <2.5. , 795(2):104.

Whitaker, K. E., Pope, A., Cybulski, R., Casey, C. M., Popping, G., and Yun, M. S. (2017). The Constant Average Relationship between Dust-obscured Star Formation and Stellar Mass from z = 0 to z = 2.5. , 850(2):208.

Whitaker, K. E., van Dokkum, P. G., Brammer, G., and Franx, M. (2012). The Star Formation Mass Sequence Out to z = 2.5. , 754(2):L29.

Wright, E. L., Eisenhardt, P. R. M., Mainzer, A. K., Ressler, M. E., Cutri, R. M., Jarrett, T., Kirkpatrick, J. D., Padgett, D., McMillan, R. S., Skrutskie, M., Stanford, S. A., Cohen, M., Walker, R. G., Mather, J. C., Leisawitz, D., Gautier, Thomas N., I., McLean, I., Benford, D., Lonsdale, C. J., Blain, A., Mendez, B., Irace, W. R., Duval, V., Liu, F., Royer, D., Heinrichsen, I., Howard, J., Shannon, M., Kendall, M., Walsh, A. L., Larsen, M., Cardon, J. G., Schick, S., Schwalm, M., Abid, M., Fabinsky, B., Naes, L., and Tsai, C.-W. (2010). The Wide-field Infrared Survey Explorer (WISE): Mission Description and Initial On-orbit Performance. , 140(6):1868–1881.

Wuyts, S., Förster Schreiber, N. M., van der Wel, A., Magnelli, B., Guo, Y., Genzel, R., Lutz, D., Aussel, H., Barro, G., Berta, S., Cava, A., Graciá-Carpio, J., Hathi, N. P., Huang, K.-H., Kocevski, D. D., Koekemoer, A. M., Lee, K.-S.,

Le Floc'h, E., McGrath, E. J., Nordon, R., Popesso, P., Pozzi, F., Riguccini, L., Rodighiero, G., Saintonge, A., and Tacconi, L. (2011). Galaxy Structure and Mode of Star Formation in the SFR-Mass Plane from z ~2.5 to z ~0.1. , 742(2):96.

York, D. G., Adelman, J., Anderson, John E., J., Anderson, S. F., Annis, J., Bahcall, N. A., Bakken, J. A., Barkhouser, R., Bastian, S., Berman, E., Boroski, W. N., Bracker, S., Briegel, C., Briggs, J. W., Brinkmann, J., Brunner, R., Burles, S., Carey, L., Carr, M. A., Castander, F. J., Chen, B., Colestock, P. L., Connolly, A. J., Crocker, J. H., Csabai, I., Czarapata, P. C., Davis, J. E., Doi, M., Dombeck, T., Eisenstein, D., Ellman, N., Elms, B. R., Evans, M. L., Fan, X., Federwitz, G. R., Fiscelli, L., Friedman, S., Frieman, J. A., Fukugita, M., Gillespie, B., Gunn, J. E., Gurbani, V. K., de Haas, E., Haldeman, M., Harris, F. H., Hayes, J., Heckman, T. M., Hennessy, G. S., Hindsley, R. B., Holm, S., Holmgren, D. J., Huang, C.-h., Hull, C., Husby, D., Ichikawa, S.-I., Ichikawa, T., Ivezić, Ž., Kent, S., Kim, R. S. J., Kinney, E., Klaene, M., Kleinman, A. N., Kleinman, S., Knapp, G. R., Korienek, J., Kron, R. G., Kunszt, P. Z., Lamb, D. Q., Lee, B., Leger, R. F., Limmongkol, S., Lindenmeyer, C., Long, D. C., Loomis, C., Loveday, J., Lucinio, R., Lupton, R. H., MacKinnon, B., Mannery, E. J., Mantsch, P. M., Margon, B., McGehee, P., McKay, T. A., Meiksin, A., Merelli, A., Monet, D. G., Munn, J. A., Narayanan, V. K., Nash, T., Neilsen, E., Neswold, R., Newberg, H. J., Nichol, R. C., Nicinski, T., Nonino, M., Okada, N., Okamura, S., Ostriker, J. P., Owen, R., Pauls, A. G., Peoples, J., Peterson, R. L., Petravick, D., Pier, J. R., Pope, A., Pordes, R., Prosapio, A., Rechenmacher, R., Quinn, T. R., Richards, G. T., Richmond, M. W., Rivetta, C. H., Rockosi, C. M., Ruthmansdorfer, K., Sand ford, D., Schlegel, D. J., Schneider, D. P., Sekiguchi, M., Sergey, G., Shimasaku, K., Siegmund, W. A., Smee, S., Smith, J. A., Snedden, S., Stone, R., Stoughton, C., Strauss, M. A., Stubbs, C., SubbaRao, M., Szalay, A. S., Szapudi, I., Szokoly, G. P., Thakar, A. R., Tremonti, C., Tucker, D. L., Uomoto, A., Vanden Berk, D., Vogeley, M. S., Waddell, P., Wang, S.-i., Watanabe, M., Weinberg, D. H., Yanny, B., Yasuda, N., and SDSS Collaboration (2000). The Sloan Digital Sky Survey: Technical Summary. , 120(3):1579–1587.

Zaw, I., Chen, Y.-P., and Farrar, G. R. (2019). A Uniformly Selected, All-sky, Optical AGN Catalog. , 872(2):134.

Apéndice A

Star Formation Rates: comparison with other Star Formation tracers in literature

In this appendix we enunciate the set of equations used in this work to derive SFRs from UV and total IR luminosities, based on independent flux measurements from the different data sets presented in section 2.2. First, we estimate UV+IR SFRs in our 2MRS-WISE sample by using eq. 12 and 13 from Wang et al. (2016), which apply an IR correction to the UV luminosities.

$$\mathrm{SFR_{FUV+IR}}/\mathrm{M_\odot\ yr^{-1}} = 1.72 \times 10^{-10}[\mathrm{L_{FUV}}/\mathrm{L_\odot} + 0.46 \times \mathrm{L_{IR}}/\mathrm{L_\odot}] \quad \text{(A0.1)}$$

$$\mathrm{SFR_{NUV+IR}}/\mathrm{M_\odot\ yr^{-1}} = 2.60 \times 10^{-10}[\mathrm{L_{NUV}}/\mathrm{L_\odot} + 0.27 \times \mathrm{L_{IR}}/\mathrm{L_\odot}] \quad \text{(A0.2)}$$

These equations (6 and 7) use a Kroupa IMF. UV and total IR SFRs have been calculated trivially from the relation of radiative flux F and luminosity L, i.e., $F = \frac{L}{4\pi d_\mathrm{L}^2}$, with d_L the luminosity distance of a given galaxy.

Due to an overestimation of our UV-luminosities by the dust attenuation correction (i.e., correction by extinction) of eq. 5 from Wang et al. (2016), we have used the non-corrected versions of luminosities $\mathrm{L_{UV}}$ to derive SFRs.

Additionally, we carry out independent calculations of SFRs using the total IR luminosities based on IRAS calibrations of the $\mathrm{f_{60\mu m}}$ and $\mathrm{f_{100\mu m}}$ FIR bands.

Specifically, we used equation (E3) from Orellana et al. (2017), as it follows:

$$\frac{F_{\rm IR}}{[\rm W/m^2]} = 1.8 \times 10^{-14} \left(1.439 \frac{f_{60}}{[\rm Jy]} + 2.450 \frac{f_{100}}{[\rm Jy]} \right) \tag{A0.3}$$

To convert from IRAS total IR luminosity to SFR we use the following expression:

$$\rm SFR_{IR}/M_{\odot}\ yr^{-1} = 1.063 \times 10^{-10}\ L_{IR}/L_{\odot} \tag{A0.4}$$

This is effectively the equation 3 of Kennicutt (1998), but the extra factor of ∼1.063 compensates for the conversion from a Chabrier IMF to a Kroupa IMF (Conroy et al., 2009) and the conversion from FIR to IR luminosities (factor 0.92). Note that eq. A0.4 is effectively the same as eq. 12 of Cluver et al. (2017), which uses a Kroupa IMF and an IR luminosity. We assess that eq. 3.3.3 is higher than the total IR SFRs calculated from eq. 12 from Kennicutt and Evans (2012) by a ∼0.14 dex offset.

Apéndice B

The Star Formation Plane according to WISE-4 band

In this appendix we show a SFP based purely on the W4 band (see Fig. A0.1). This diagram shows W4-based SFRs as a function of stellar mass, and the same MS of Fig. 3.4.1 being displayed for comparison. We see similar shapes in contours, which is the expected tight correlation for W3 and W4 as it has been shown by Cluver et al. (2017). One important difference between W3 and W4 MS is the bulk that is formed mostly in the high mass end of the MS, where we see a clear overlap between black, red and green contours, i.e., confusion between the different morphologies. In general, W3 and W4 SFRs show similar trends for both, low mass end and for the high mass end, although with an offset for the mean SFRs of $\sim$0.2 dex between W3 and W4 SFRs of the pure-spiral galaxies. In addition, the MS based on W4 band has a flatter slope with roughly constant SF in the high mass end. An offset spanning from 0 to ~ -0.2 dex must be considered in the W4-based SFRs, for consistency with other SF tracers (further details in section 3.3).

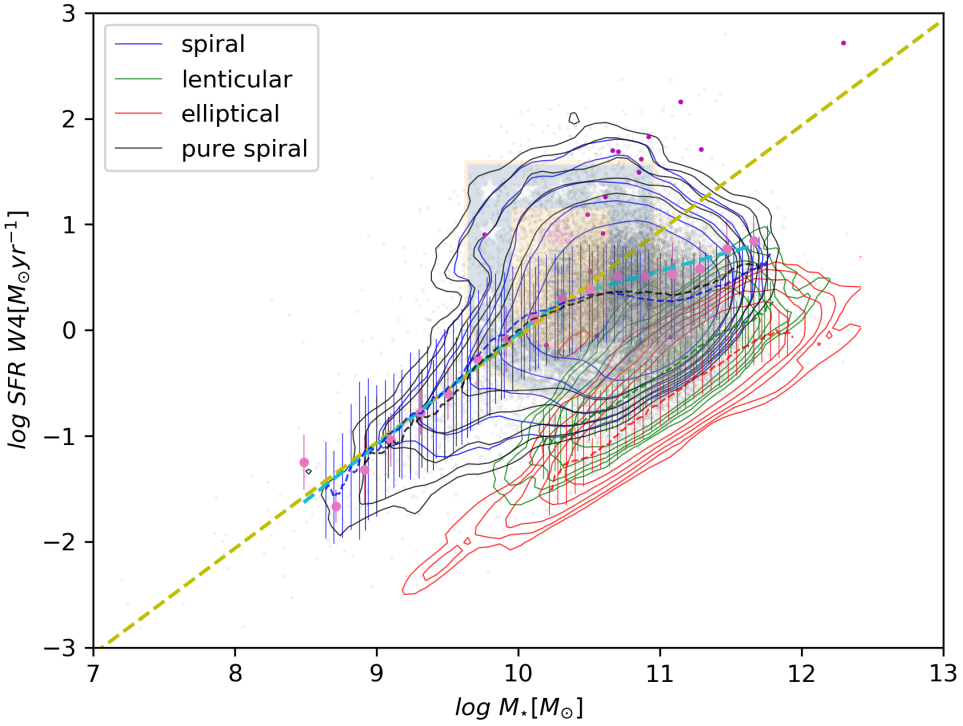

Figura A0.1: Star Formation Plane (SFP) using SFRs from a WISE-4 band calibration, the description is the same as in Fig. 3.4.1.

Apéndice C

Unusual objects

In this appendix we want to show some examples where galaxies were wrongly classified by their 2MRS morphology (Huchra et al., 2012), hence we probe here that our morphological classification based on WISE colors can contradict the 2MRS morphology. For this purpose we first test the reliability of the 2MRS morphology by visually examining 6 specific 2MRS types in the SDSS DR15 image query: type −5 (elliptical galaxies, morphology E5) and those with types 5 and 4 (barred spirals, type Sc and Sbc respectively), plus the 2 limits of the transition types, S0 (type 0) and E0 (type −4). We recall that our color cutoffs from our WISE classification correspond to W2−W3=0.7 and W2−W3=1.4 (see main text).

First, we divide our sample of 2MRS-WISE galaxies in different lists depending on their WISE color classification, with colors cutoffs to be specified in the following. Here we set conservative cutoffs of W2−W3=0.5 and W2−W3=3, aiming to ensure that we will find only well-defined morphologies. Thus, we classify galaxies as spirals by their colors W2−W3>3, or as ellipticals if they have colors W2−W3<0.5. In the case of Sc/Sbc spirals, we set a secondary limit of W2−W3=1, which is roughly the limit where ellipticals and spirals overlap in the WISE color-color diagram of Jarrett et al. (2011), implying that W2−W3=1 is a transition limit where we expect to find mostly well-defined lenticulars and/or dusty spirals. Due to a small size of the Sbc spiral sample (less than 20 objects in both limits), we have included some Sc type spirals in the same sample of Sbc spirals.

As a second step, we perform an online search of our listed 2MRS-WISE galaxies

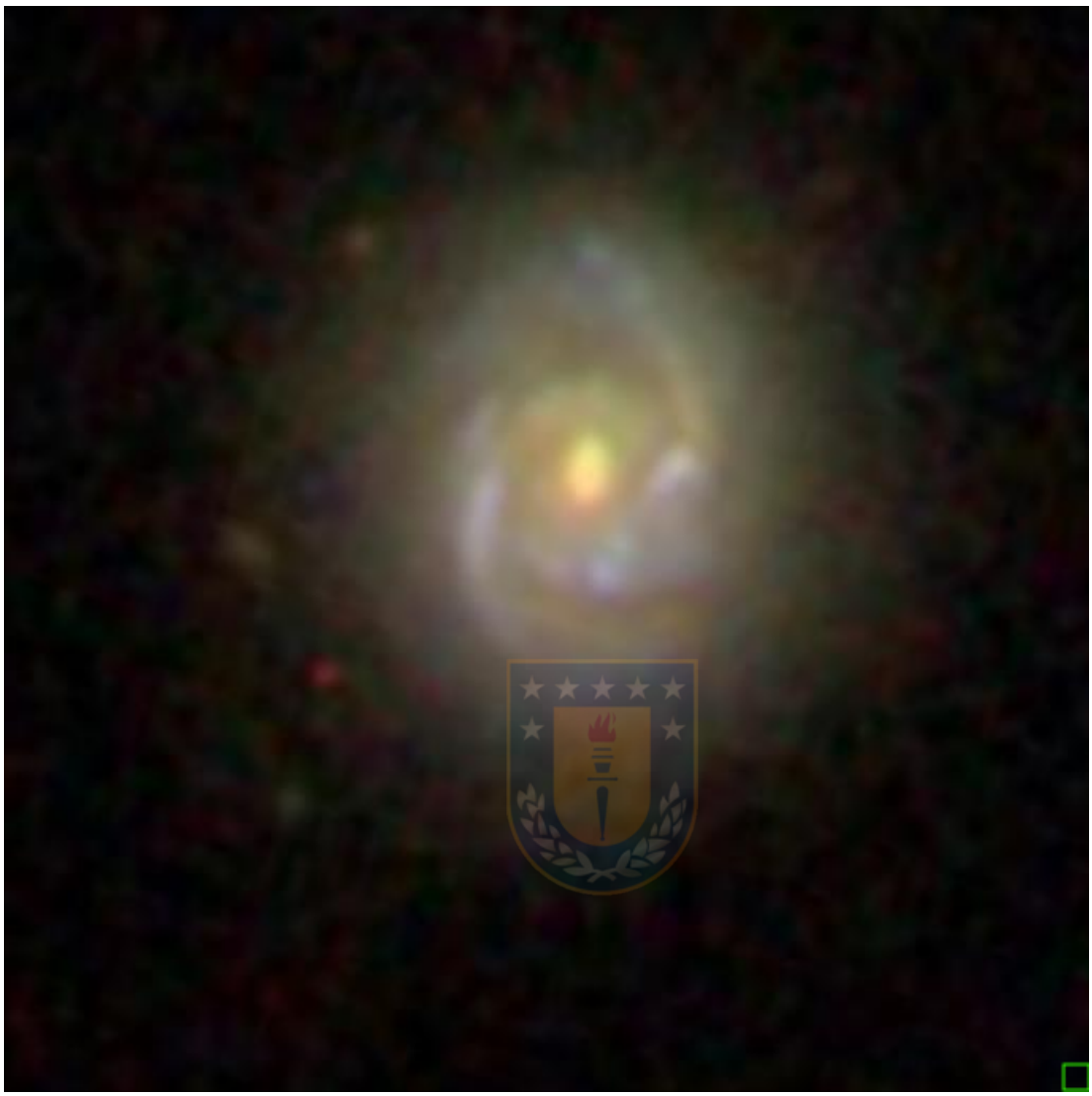

Figura A0.1: SDSS DR15 image of J104809.32+481953.5 showing a spiral and late-type spectrum, in contradiction with its 2MRS type -5 of E5 elliptical.

on the DR15 web page, keeping only the sources with a Declination $> -10°$. These lists of galaxies start roughly with 100 galaxies but is reduced to a size of $\sim$50 images due to mismatches in the astrometry with 2MRS. Then, we check out if these galaxies effectively match to the morphologies displayed in their SDSS images. We found that 2MRS ellipticals (type -5) with colors W2$-$W3$<$0.5 have the correct morphology (i.e. they look like dusty spheroids with very few ellipticity), but at redder colors (W2$-$W3$>$3), the morphology of these assumed ellipticals correspond to spirals, therefore we determine that such galaxies were wrongly classified by the 2MRS morphology. Specifically, such wrong examples of ellipticals appear in their SDSS images having the usual spiral arm pattern,

with some exceptions that arise from the extinction effects present in the ugriz filters of the SDSS survey. In Fig. A0.1 we show an example of 2MRS galaxy with a wrong morphology, this corresponds to a galaxy classified as elliptical (type -5) by 2MRS but that was defined as spiral by their WISE colors; in this case a spiral morphology is the correct classification, consistent with its late-type DR15 spectrum.

For the Sc spirals, we perform a search imposing the color limit W2$-$W3$<$0.5, that is proper of ETGs, and conservative color cutoff of W2$-$W3$>$3, proper of spiral galaxies. We found that for redder colors W2$-$W3$>$3 the images of these 2MRS Sc spirals are morphologically correct, showing clear spiral arms and a well defined nucleus. Conversely, if we change to bluer colors (W2$-$W3$<$0.5), we observe mostly unexpected dusty halos with lenticular shapes, and we attribute this problem to extinction effects on SDSS filters. Therefore, here we have the opposite to the first example: an object wrongly classified as Sc spiral by 2MRS has been visually confirmed as an elliptical by its DR15 image and early-type spectrum, as it is shown in Fig. A0.2. In the case of 2MRS Sbc types, we obtained the same results as in Sc types. Additionally, we investigate Sc/Sbc spirals close to the limit W2$-$W3=1, where we see mostly dusty lenticular shapes below and bluer spiral shapes above this color limit, suggesting this is a sharp limit to classify our spiral galaxies by colors.

Now we test transition morphologies on DR15 corresponding to SO and EO galaxies. SO (2MRS type 0): we only see lenticular morphologies (plus very few ellipticals) in colors W2$-$W3$<$0.5, and blue spirals for W2$-$W3$>$3 colors, so we have that type 0 fails in describing galaxies at lower WISE colors where we expect to find mostly elliptical galaxies. EO (type -4): colors with W2$-$W3$<$0.5 only show elliptical morphologies (plus a few lenticulars), whilst W2$-$W3$>$3 colors only show spiral morphologies, although the size of the latter is relatively small ($<<$100 sources). Thus, we confirm that 2MRS morphology fails in some cases, like type 0 galaxies at lower colors or type -4 at higher colors.

Thus, from the previous ideas presented in this section, we confirm our assumption that the 2MRS morphology is unreliable, since its classification fails in some cases, when we check their DR15 images. Hence, we use our own method based on WISE colors to make a more reliable classification of the 2MRS galaxies.

Figura A0.2: SDSS DR15 image of J081002.49+225141.6 showing a lenticular/elliptical and early-type spectrum, in contradiction with its 2MRS type 4 of Sbc spiral.